

Electronic Supplementary Material (ESI) for Energy & Environmental Science.

Supporting information for

Ultrahigh solar-driven atmospheric water production enabled by scalable rapid-cycling water harvester with vertically aligned nanocomposite sorbent

Jiaxing Xu[†], Tingxian Li^{,†}, Taisen Yan[†], Si Wu, Jingwei Chao, Minqiang Wu, Xiangyan Huo, Pengfei Wang, Ruzhu Wang^{*}*

Research Center of Solar Power & Refrigeration, School of Mechanical Engineering, Shanghai Jiao Tong University, Shanghai 200240, China.

[†] These authors contributed equally to this work

* E-mail: Litx@sjtu.edu.cn; rzwang@sjtu.edu.cn.

This file includes:

Supplementary Note 1–2

Supplementary Figures S1 – S48

Supplementary Tables S1 – S6

References

Table of contents

Supplementary Note 1. Theoretical models and simulation of water sorption-desorption of the vertically aligned graphene aerogel nanocomposite sorbent.

Supplementary Note 2. Energy balance analysis of the solar-driven atmospheric water harvester.

Figure S1. Molds for directional freezing casting.

Figure S2. Optimization of the ratio of GO and SA.

Figure S3. Optical images of pure porous GO matrix, pure porous SA matrix, and water stability tests of pure GO matrix.

Figure S4. Stress-strain curves of matrixes and composite sorbent showing the cross-linking of SA is vital to enhancing the mechanical strength of this porous matrix.

Figure S5. The suggested concentration of LiCl solution used to preparing nanocomposite sorbent for avoiding salt solution leakage under different humidity conditions at 30 °C.

Figure S6. Optical photos showing the change of morphology after cross-linking and salt process.

Figure S7. Elemental mapping with EDX showing the uniformly distribution of LiCl in GO-SA matrix.

Figure S8. SEM image showing the LiCl exists in the form of 200-900 nm scale cubic salt particles, confining in rGO-SA matrix.

Figure S9. SEM images showing the morphology of LiCl@rGO-SA after 10 times water sorption-desorption cycles in SAWH device.

Figure S10. Phase diagram of LiCl-water vapor.

Figure S11. Schematic diagram of the water vapor generating system of thermogravimetric analyzer (STA 449, Netzsch) equipped with a moisture humidity generator (MHG 32, ProUmid).

Figure S12. The ambient conditions (Temperature and relative humidity of air) of a typical day in each month at arid regions of Kharga, Yazd, Oodnadatta, and Minfeng.

Figure S13. Optical photos showing change of morphology during the water sorption process.

Figure S14. The TGA curves showing the dynamic water sorption process of GO-SA matrixes before and after cross-linking under testing condition of under 30°C, 1.2 kPa (30% RH) for sorption and 90 °C, 4.2 kPa for desorption.

Figure S15. TG-DSC (coupled thermogravimetric and differential scanning calorimetric analysis) curves showing the dynamic water sorption-desorption process of LiCl@rGO-SA under working condition of 30% RH, 30 °C for sorption and 6.0% RH, 90 °C for desorption.

Figure S16. Repeated water sorption-desorption cycling tests of nanocomposite sorbent under 30°C, 70% RH for sorption and 90 °C for desorption.

Figure S17. Photos of the nanocomposite sorbent, LiCl@rGO-SA, reaching sorption equilibrium under 30°C, 70% RH and 30°C, 90% RH.

Figure S18. Contact angles of GO, GO-SA, Cross-linked GO-SA, and LiCl@rGO-SA with water droplet.

Figure S19. Schematic showing the structure and static force balance of the hanging vertically aligned composite sorbent with captured water.

Figure S20. The maximum height of trapped water without leakage for composite sorbent with different pore radius and contact angles.

Figure S21. The optical images showing the pore structures of LiCl@rGO-SA_unordered.

Figure S22. Optical photo of the water sorption-desorption kinetics testing device (Top photo of sorption, bottom photo of desorption).

Figure S23. The simulated adsorption/desorption rates evolutions for different cases.

Figure S24. The simulated water vapor concentrations evolutions of bulk concentration (C_{amb}), surface concentration (C_{surf}), intra-concentration (C_{sorb}), and equilibrium concentration ($C_{sorb,eq}$) during water sorption-desorption process.

Figure S25. The simulated evolutions of sorbent temperatures during water sorption-desorption process.

Figure S26. Structures of the compact semi-active SAWH device.

Figure S27. The photos of PV panel and the air fan.

Figure S28. The air flow speeds in the SAWH device under different solar irradiation intensities.

Figure S29. The light absorbance of LiCl@rGO-SA and commercial selective solar absorber over a wide spectrum range from 250 nm to 15 μm .

Figure S30. The solar collection temperatures of commercial selective absorber and LiCl@GO-SA under a natural solar irradiation of 900-1000 W/m^2 .

Figure S31. The photos of the sorbent unit.

Figure S32. Structure illustration of the compact water condenser.

Figure S33. Thermal analysis of the water desorption-condensation process for the compact SAWH device.

Figure S34. The temperature evolutions of sorbent, condenser, and ambient air for the SAWH without installing an insulated panel between sorbent and condenser under a stable solar irradiation of 950 W m^{-2} .

Figure S35. a. The geometric construction of device without insulating panel. b. The geometric construction of device with insulating panel.

Figure S36. The simulation results of water release-condensation process.

Figure S37. The evolutions of sample temperatures at center points (data extracted from infrared temperature mapping).

- Figure S38.** Photo of SAWH testing under laboratory condition (0.95-1.05 kW/m² solar irradiation).
- Figure S39.** The spectra of sunlight and xenon lamp, and the transmissivity of the acrylic cover.
- Figure S40.** The contact angle of hydrophilic PET membrane with a water droplet.
- Figure S41.** Photos of condensation surface with/without waterproof membrane during water harvesting process.
- Figure S42.** The changes of liquid level of collected water in the silicone tube showing the volume changes of collected water during a typical outdoor water collection cycle.
- Figure S43.** Temperature evolution of the water-released sorbent during its initial phase of air cooling and water sorption.
- Figure S44.** The changes of relative humidity of local ambient air on August 17, 2020.
- Figure S45.** The mass transport balance during desorption-condensation process for the compact SAWH device.
- Figure S46.** Optical photos showing the shape of the nanocomposite sorbent before and after ~10 times SAWH cycles in device.
- Figure S47.** Schematic showing an automatic operation strategy for continuous water production.
- Figure S48.** Schematic showing the automatic SAWH device with added mechatronic components.
- Table S1.** The testing conditions of the LiCl@rGO-SA and other reported composite sorbent during the dynamic water sorption tested by commercial water sorption instrument.
- Table S2.** Thermal efficient analysis for the SAWH device with/without insulation panel.
- Table S3.** The mass and thickness of the four sorbent units in SAWH device.
- Table S4.** The water harvesting capacity of the SAWH device in the view of sorbent, mass of device, volume of device, and solar collection surface of device.
- Table S5.** Concentration of primary metal elements in collected water measured by ICP-OES.
- Table S6.** Concentration of possible ions in collected water measured by Ion Chromatography.
- Video S1.** Shaking Sorbent Showing Its Stability.
- Video S2.** Atmospheric Water Harvesting Process Without Waterproof Membrane.
- Video S3.** Atmospheric Water Harvesting Process With Waterproof Membrane.

Supplementary Note 1. Theoretical models and simulation of water sorption-desorption of the vertically aligned graphene aerogel nanocomposite sorbent.

The water sorption process of the sorbent generally includes three steps: (i) external surface vapor diffusion between air and the top surface of the sorbent; (ii) internal vapor diffusion from the top surface to salts; and (iii) the reaction, deliquescence, or solution absorption of salts. The heat and mass transfer models of the water sorption/desorption process were introduced to simulate the dynamics process and to analyze the resistances of kinetics. The numerical simulation models are developed based on the following assumptions:

- (i) The pore structure and salt distribution are assumed homogeneous within the sorbent layer.
- (ii) The convective transport by the pressure difference between inner sorbent and bulk air is neglected.
- (iii) The porosity of the composite sorbent is change with the water uptake. To simplify the simulation, the porosity is not included inside the partial derivative of time. The porosity-dependent effective diffusivity is considered.
- (iv) The tortuosity of LiCl@rGO-SA with vertical aligned pore structures is assumed to 1.
- (v) The LDF model is adopted to predict the sorption rate, the reaction coefficient of sorption and desorption are optimized from the sorption and desorption curves respectively. The reaction coefficients are assumed to keep constant during the whole sorption/desorption process.

The mass and heat models are shown as following:

Sorbent layer ($0 < z < \delta_s$):

$$\frac{\partial c_s}{\partial t} - \nabla \cdot D_{eff} \nabla C + \frac{1 - \varepsilon_s}{\varepsilon_s} \rho_s \frac{\partial q}{\partial t} = 0 \quad (S1)$$

$$\rho C_p \frac{\partial T_s}{\partial t} - \nabla \cdot \lambda_s \nabla T_s - \rho_s \frac{\partial q}{\partial t} \Delta h_r = 0 \quad (S2)$$

Air-sorbent interface ($z = \delta_s$):

$$\left. \frac{\partial c_s}{\partial z} \right|_{z=\delta_s} = h_m (C_s - C_a) \quad (S3)$$

$$\left. \frac{\partial T_s}{\partial z} \right|_{z=\delta_s} = h_T (T_s - T_a) \quad (\text{S4})$$

Position of the support plate (Aluminum sheet) ($z=0$):

$$\frac{\partial c}{\partial z} = 0, \frac{\partial T}{\partial z} = 0 \quad (\text{S5})$$

The initial conditions:

$$c|_{t=0} = c_0, T|_{t=0} = T_0 \quad (\text{S6})$$

Where c_s is the vapor concentration in nanocomposite adsorbent (g m^{-3}), ε_s is the porosity of nanocomposite sorbent varying with the water sorption, $\varepsilon_s = \varepsilon_{s,0} - q \cdot \frac{\rho_{s,dried}}{\rho_{water}}$, wherein q is the time-varied amount of adsorbed water (g g^{-1}) and $\varepsilon_{s,0}$ represents the initial porosity of totally dried nanocomposite sorbent, and $\rho_{s,dried}$ is the density of totally dried nanocomposite adsorbent (g m^{-3}). In this simulation, the porosity of LiCl@rGO-SA changes from 0.92 to 0.71 during the water uptake process at 30% RH. ρ_{water} is the density of pure water (g m^{-3}). The D_{eff} is the effective diffusivity coefficient ($\text{m}^2 \cdot \text{s}^{-1}$), which is determined by the molecular diffusivity of water vapor in the air (D_m , $\text{m}^2 \cdot \text{s}^{-1}$), porosity (ε), and tortuosity (τ) as following:

$$D_m(T, P) = 1.758 \times 10^{-4} \frac{(T + 273.15)^{1.685}}{P_0} \left(\frac{\text{m}^2}{\text{s}} \right) \quad (\text{S7})$$

$$D_{eff} = \frac{\varepsilon}{\tau} \cdot D_m \quad (\text{S8})$$

The reaction rate of salt with water vapor is described by the linear driving force model (LDF) as following equation,

$$\frac{\partial q}{\partial t} = k_{LDF} (c_e - c) \quad (\text{S9})$$

where k_{LDF} represents the reaction coefficient ($\text{m}^3 \text{g}^{-1} \text{s}^{-1}$) obtained by the fitting from the sorption curves. Considering the multi-step water desorption mechanism, the single coefficient k_{LDF} was replaced by three kinetics coefficients, k_{chem} , k_{cryst} , and k_{evap} , representing the desorption kinetic coefficient at different stages of chemical desorption ($0 \leq q < q_{chem}$), crystallization (q_{chem}

$\leq q < q_{\text{deli}}$), and solution evaporation ($q > q_{\text{deli}}$), respectively ($\text{m}^3 \text{g}^{-1} \text{s}^{-1}$). C_e represents the concentration of water sorption after the reaction reaches equilibrium (g m^{-3}).

For the parameters of heat transfer, T_s represents the temperature of nanocomposite adsorbent ($^{\circ}\text{C}$). ρC_p is the heat capacity of the nanocomposite adsorbent ($\text{J m}^{-3} \text{K}^{-1}$), $\rho C_p = \rho_s \cdot (C_{p,s} + q \cdot C_{p,H_2O})$, wherein $C_{p,s}$ and C_{p,H_2O} is the specific heat capacity of nanocomposite and water ($\text{J g}^{-1} \text{K}^{-1}$). The specific heat capacity of adsorbent is $1.2 \text{ J g}^{-1} \text{K}^{-1}$ measured by DSC. λ_s is the thermal conductivity coefficient of the sorbent, $0.2 \text{ W m}^{-1} \text{K}^{-1}$, gained by hot disk. Δh_r is the enthalpy of adsorption with the value to (47 kJ mol^{-1} or 2611 J g^{-1} , an average value of chemical reaction and deliquescence). h_m , h_T are the mass and heat transfer coefficient (m s^{-1} and $\text{W m}^{-2} \text{K}^{-1}$), which are calculated by following equations:

$$h_m = D_z (2.0 + 0.6 \text{Re}^{1/2} \text{Sc}^{1/3}) / \delta \quad (\text{S10})$$

$$h_T = \lambda_a (2.0 + 0.6 \text{Re}^{1/2} \text{Pr}^{1/3}) / \delta \quad (\text{S11})$$

As we discussed above, the transport resistances for vapor transport from ambient air to reactive salt can be divided as transport resistance in extra-surface (R_{surf} , s m^{-1}), transport resistance in pores (R_{diff} , s m^{-1}), and reaction resistance between reactive salt and vapor (R_{react} , s m^{-1}), which can be calculated as following equations:

$$R_{\text{surf}} = \frac{C_{\text{amb}} - C_{\text{surf}}}{\dot{m}/A}, \quad R_{\text{surf}} = \frac{1}{h_m} \quad (\text{S12})$$

$$R_{\text{diff}} = \frac{C_{\text{surf}} - C_{\text{sorb}}}{\dot{m}/A}, \quad R_{\text{diff}} = \frac{\delta}{D_{\text{eff}}} \quad (\text{S13})$$

$$R_{\text{react}} = \frac{C_{\text{sorb}} - C_{\text{sorb,eq}}}{\dot{m}/A}, \quad R_{\text{react}} = \frac{1}{\delta_s \rho_s K_{\text{LDF}}} \quad (\text{S14})$$

We first obtained the time-varied concentrations of water vapor at different positions (C_{surf} , C_{sorb} , and $C_{\text{sorb,eq}}$) represent water concentration of nanocomposite surface, salts, and salts reaching sorption equilibrium, respectively) and water sorption rates (\dot{m}) (see following Figure 13, 14) according to the above mentioned mathematic models, solved by a commercial software of COMSOL Multiphysics.

Supplementary Note 2. Energy balance analysis of the solar-driven atmospheric water harvester.

The structure of the water harvester is schematically shown in **Figure 4a**, **4b**, and **Supplementary Figure 26**, which consists of a solar absorber to capture solar thermal, an acrylic cover to weaken the convective and radiative heat loss to ambient, and a condenser enhanced by forced convection assisted cooling. For the photo-thermal parts, selective absorptive layer (high absorptivity at solar spectrum and low emissivity at far-infrared band) is used to enhance solar photo-thermal ability and reduce the radiative heat loss, simultaneously. The adsorbent is coated on the back side of selective absorptive layer. The thermal balance during water release process (without installing an insulation panel between sorbent and condenser) in the view of sorbent, can be described as following equation:

$$(1-f) \cdot \alpha \cdot q_{\text{solar}} = q_{\text{radi,cover}} + q_{\text{conv,cover}} + q_{\text{radi,condenser}} + q_{\text{conv,condenser}} + m \cdot h_r \quad (\text{S15})$$

where q_{solar} , $q_{\text{radi,cover}}$, $q_{\text{conv,cover}}$, $q_{\text{radi,condenser}}$, and $q_{\text{conv,condenser}}$ represent the heat flux of input solar irradiation, radiative and convective heat flux of acrylic cover to ambient, radiative and convective heat flux from the sorbent to the condenser (W m^{-2}), respectively. The f is the sum of reflectivity and absorbance ratio of acrylic cover, α is the absorptivity of the selective solar absorber, m is the mass of desorbed water (g), and Δh_r is the sorption enthalpy (kJ mol^{-1}).

For heat loss through acrylic cover to ambient:

$$q_{\text{radi,cover}} = \varepsilon_{\text{cover}} \cdot (T_{\text{cover,out}}^4 - T_{\text{amb}}^4) \quad (\text{S16})$$

$$q_{\text{conv,cover}} = h_{\text{conv,cover}} \cdot (T_{\text{cover,out}} - T_{\text{amb}}) \quad (\text{S17})$$

For heat loss through sorbent to condenser:

$$q_{\text{radi,condenser}} = \varepsilon_{\text{adsorb}} \cdot (T_{\text{adsorb}}^4 - T_{\text{condenser}}^4) \quad (\text{S18})$$

$$q_{\text{conv,condenser}} = h_{\text{conv,condenser}} \cdot (T_{\text{adsorb}} - T_{\text{condenser}}) \quad (\text{S19})$$

$$\eta = \frac{\dot{m} \cdot \Delta h_r}{q_{\text{solar}}} \quad (\text{S20})$$

ϵ_{adsorb} , ϵ_{cover} are the emissivity of adsorbent and acrylic cover. $T_{cover,out}$, T_{amb} , T_{adsorb} , $T_{condenser}$ are the temperatures of extra-surface of acrylic cover, ambient, sorbent, and condenser, respectively ($^{\circ}\text{C}$). \dot{m} represents the mass flux of desorbed water (g s^{-1}) and Δh_r represents the sorption enthalpy (kJ mol^{-1}).

The values of physical properties and above-mentioned parameters are listed in following Table S2. The temperature in the out surface of acrylic cover is estimated to 40°C from the experimental data. As can be seen, there is a large heat loss from sorbent to condenser mainly through radiative heat transfer due to the large temperature difference between adsorbent and condenser. Thus, an insulator is placed between sorbent and condenser to suppress the radiative and convective heat transfer. The energy balance equations of water release process (with installing an insulation panel between sorbent and condenser) can be described by following equations:

$$(1-f) \cdot \alpha \cdot q_{solar} = q_{radi,cover} + q_{conv,cover} + q_{radi,insul} + q_{cond,insul} + m \cdot h_r \quad (\text{S21})$$

$$q_{radi,insul} = \epsilon_{adsorb} \cdot (T_{adsorb}^4 - T_{insul}^4) \quad (\text{S22})$$

$$q_{cond,insul} = \frac{(T_{adsorb} - T_{cond,in})}{\frac{\delta_{air,a}}{\lambda_{air}} + \frac{\delta_{insul}}{\lambda_{insul}} + \frac{\delta_{air,c}}{\lambda_{air}} + \frac{1}{h_{conv,condenser}}} = \frac{(T_{adsorb} - T_{insul,a})}{\frac{\delta_{air,l}}{\lambda_{air}}} \quad (\text{S23})$$

Where $q_{radi,insul}$ and $q_{cond,insul}$ are the radiative and conductive heat flux from sorbent to insulator respectively (W m^{-2}). $T_{insul,a}$ is the temperature of insulation ($^{\circ}\text{C}$). λ_{air} and λ_{insul} are the thermal conductivity of air and insulator ($\text{W m}^{-1} \text{K}^{-1}$). δ_{air} and δ_{insul} are the thicknesses of air layer and insulator layer (mm). The detailed values of above parameters can be found in following Table S2. According to the energy balance analysis, we conclude the installing of insulation panel between sorbent and condenser can efficiently reduce the heat loss from sorbent to condenser, improving the thermal efficiency of SAWH from 48.3% to 58.4%.

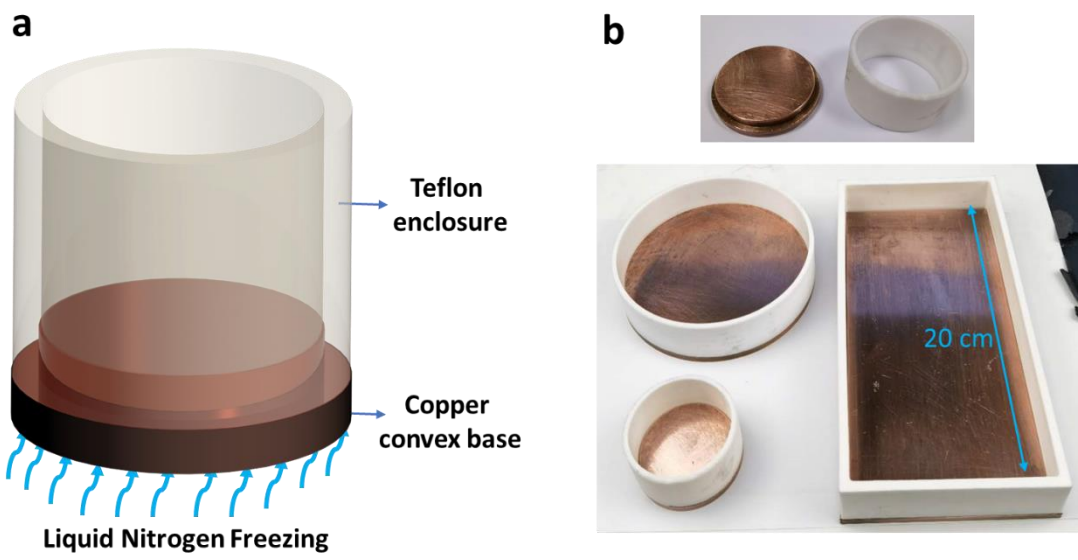


Figure S1. Molds for directional freezing casting.

(a) Schematic of the mold's structure. The mold consists of two parts: the Teflon enclosure tube and copper base, the Teflon enclosure works for the thermal insulation and the copper base works as the thermal conduction channel when the bottom touch with liquid nitrogen. As result of the vertically directional cold flow, the ice crystals grow in the vertical direction inducing vertically aligned pores after the ice is removed by vacuum drying.

(b) Optical photos of molds with different size and shapes.

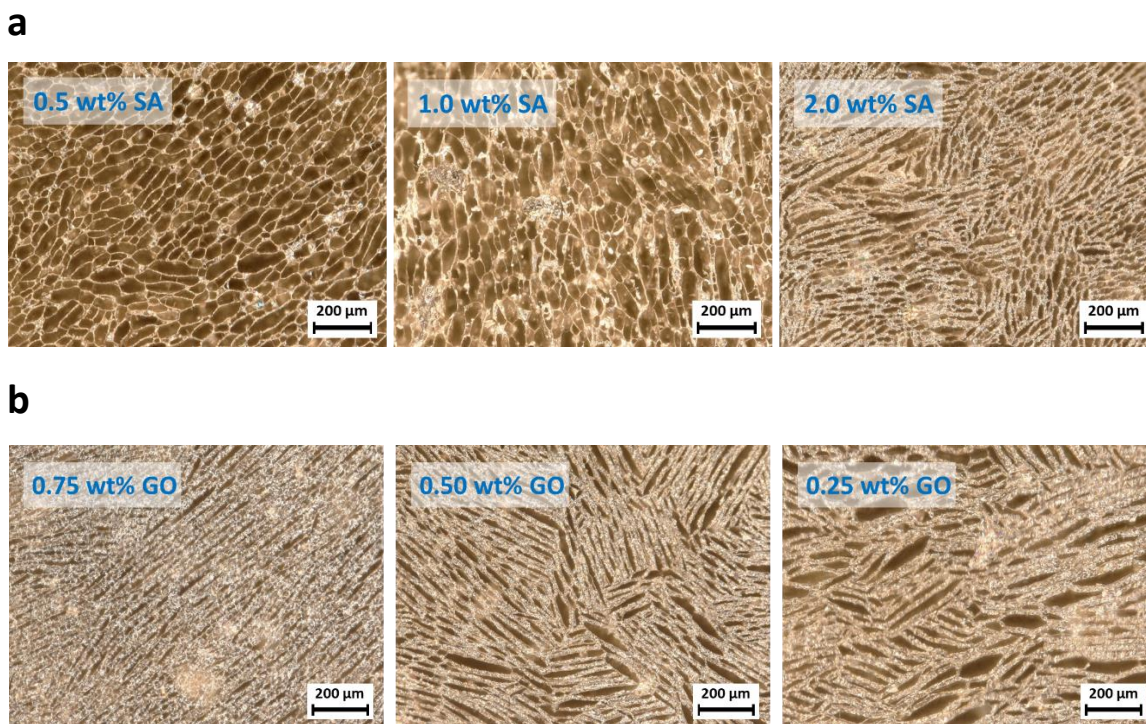


Figure S2. Optimization of the ratio of GO and SA.

(a) Optical microscope photographs of GO-SA prepared by different concentration of SA suspension but same concentration of GO suspension of 0.25 wt%. It can be conclude that the GO nanosheets make up the skeleton of the nanocomposite matrix while SA coated on the surface of GO. Although the matrix with low content of SA shows more pores but its mechanical strength is too low to load salts. We find the matrix with 2 wt% SA is strong enough for using.

(b) Optical microscope photographs of GO-SA prepared by different concentration of GO suspension but same concentration of SA suspension of 2 wt%. These three images show that the pore diameter highly depends on the concentration of GO suspension. The pore size decreased as the GO concentration increased as result of the increased crosslinking points at higher GO concentrations. Therefore, we select the optimal concentrations of SA suspension and GO suspension as 2.0 wt% and 0.25 wt%.

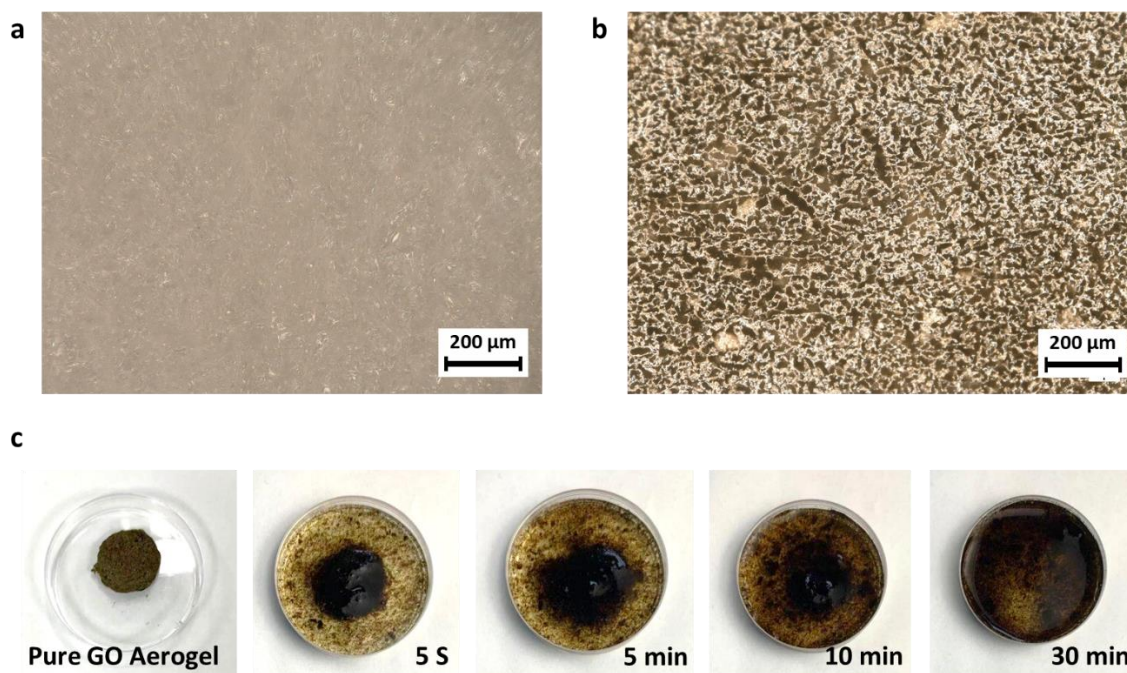


Figure S3. Optical images of pure porous GO matrix, pure porous SA matrix, and water stability tests of pure GO matrix.

(a) Optical microscope photograph of pure porous SA matrix without GO. The vertical aligned pores are not found, indicating the pure SA cannot self-assemble to be directional pores.

(b) Optical microscope photograph of pure porous GO matrix without SA. Although many pores are found, the walls of them are discontinuous and fragile, indicating the pure GO matrix is not as robust as enough.

(c) The change of pure GO matrix without SA when soaking in water. The fast solution of matrix indicates the low structure stability of pure GO matrix.

According to the above morphology of pure GO matrix and pure SA, it can be concluded that both pure GO and pure SA cannot grow to be vertical aligned pores during directional freezing process, confirming the GO-SA composite matrix brings synergetic effects of GO and SA for strengthening the structure stability.

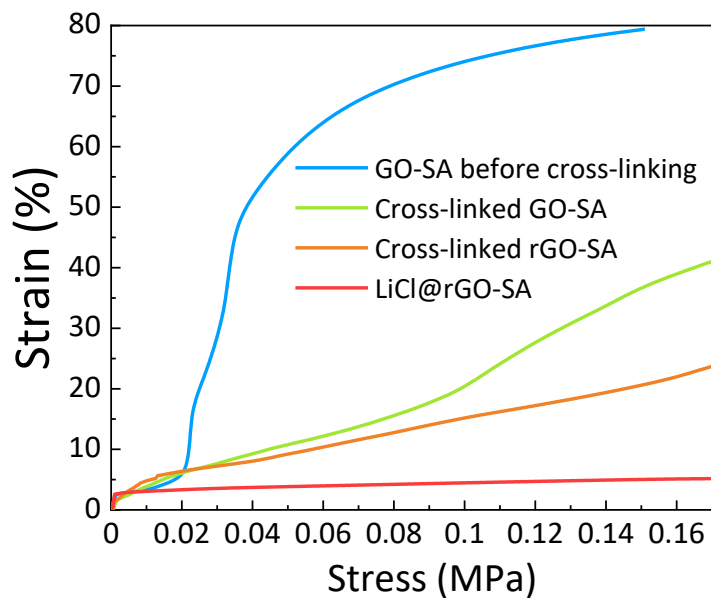


Figure S4. Stress-strain curves of matrixes and composite sorbent showing the cross-linking of SA is vital to enhancing the mechanical strength of this porous matrix.

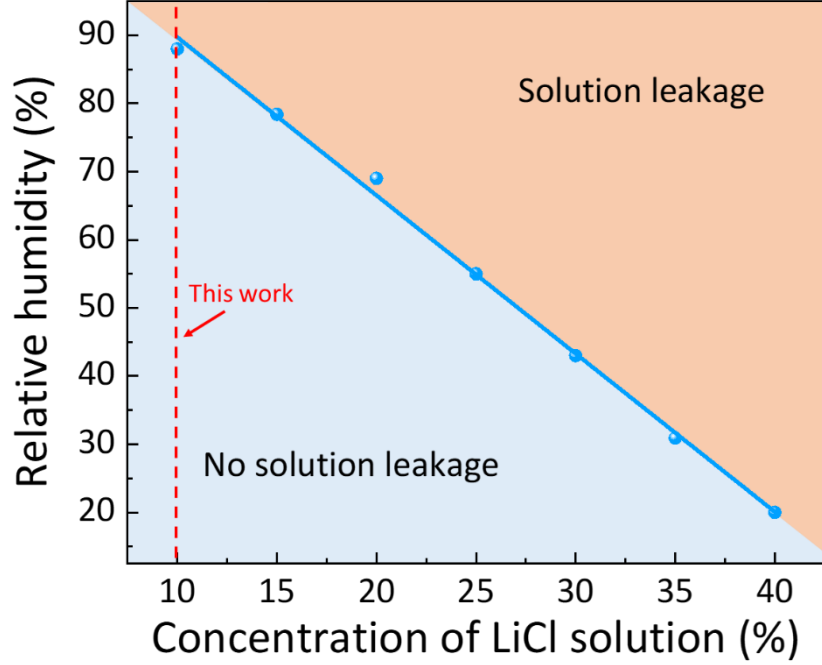


Figure S5. The suggested concentration of LiCl solution used to preparing nanocomposite sorbent for avoiding salt solution leakage under different humidity conditions at 30 °C.

The precondition of non-solution leakage is that the volume of salt solution (V_{solution}) after reaching sorption equilibrium is smaller than the pore volume of composite sorbent (V_{pore}),

$$V_{\text{solution}} < V_{\text{pore}} \quad (\text{S24})$$

The V_{solution} depends on the salt content and the working conditions, wherein the salt content (m_{LiCl}) is determined during materials preparation process, can be described by,

$$m_{\text{LiCl}} = \rho_{\text{sol,prep}} V_{\text{pore}} C_{\text{sol,prep}} \quad (\text{S25})$$

where the $\rho_{\text{sol,prep}}$ presents the density of LiCl solution used in materials preparation process and the $C_{\text{sol,prep}}$ presents the mass concentration of LiCl solution used in materials preparation process. Then, the V_{solution} can be obtained according to the salt content and its final water sorption state of solution density and concentration, as described by

$$V_{\text{solution}} = \frac{m_{\text{LiCl}}}{C_{\text{sol,sorp}} \rho_{\text{sol,sorp}}} \quad (\text{S26})$$

where the $\rho_{\text{sol,sorp}}$ presents the density of LiCl solution after reaching sorption equilibrium and the $C_{\text{sol,sorp}}$ presents the mass concentration of LiCl solution after reaching sorption equilibrium. According to above equations, the Eq. S24 can be transferred to be,

$$\frac{C_{\text{sol,prep}} \rho_{\text{sol,prep}}}{C_{\text{sol,sorp}} \rho_{\text{sol,sorp}}} < 1 \quad (\text{S27})$$

The $C_{\text{sol,sorp}}$ is determined by the relative humidity and temperature during water sorption press. Data points in Figure S5 show the relationship between $C_{\text{sol,sorp}}$ and relative humidity at 30 °C. For example, the $C_{\text{sol,sorp}}$ of LiCl solution is 10 wt% at ~90% RH. So, if we choose a salt solution with a lower mass concentration than 10 wt% during composite sorbent preparation process, the Eq. S27 can always be hold until the working condition of RH above 90%. Above conclusions are also available for other composite sorbents using LiCl regardless of the pore volume of porous matrix. We would like to mention that above analysis and calculation are under the assumptions of the water sorption capacity only comes from the LiCl and the pore volume of sorbent not apparently changed during water sorption-desorption cycles.

This figure tells us that it is necessary to choose a low solution concentration during preparation process to avoid the salt solution leakage if the sorbent exposed to a high RH moisture. In this work, we choose a low concentration of only 10 wt% to prepare the nanocomposite sorbent, which theoretically has no solution risks until the RH as high as 90%.

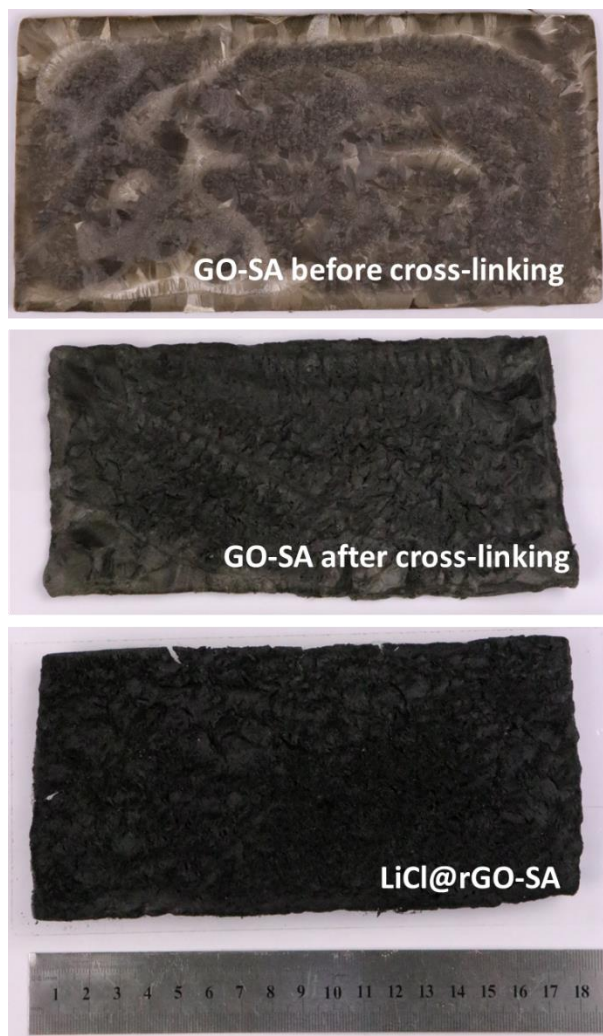


Figure S6. Optical photos showing the change of morphology after cross-linking and salt process.

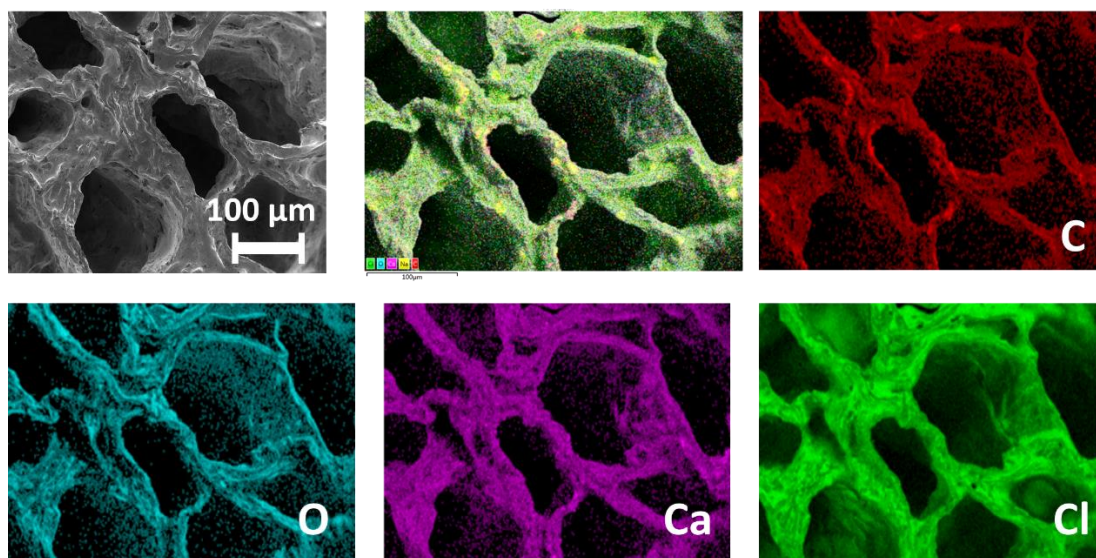


Figure S7. Elemental mapping with EDX showing the uniformly distribution of LiCl in GO-SA matrix.

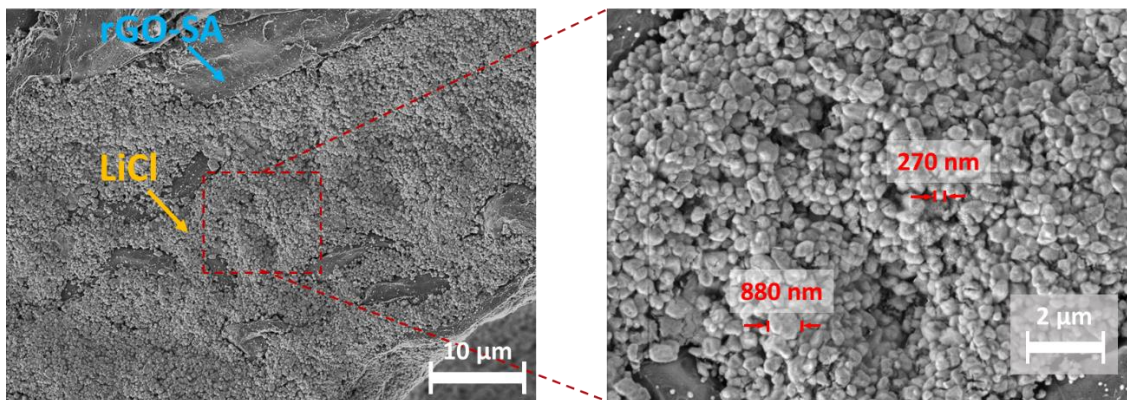


Figure S8. SEM image showing the LiCl exists in the form of 200-900 nm scale cubic salt particles, confining in rGO-SA matrix.

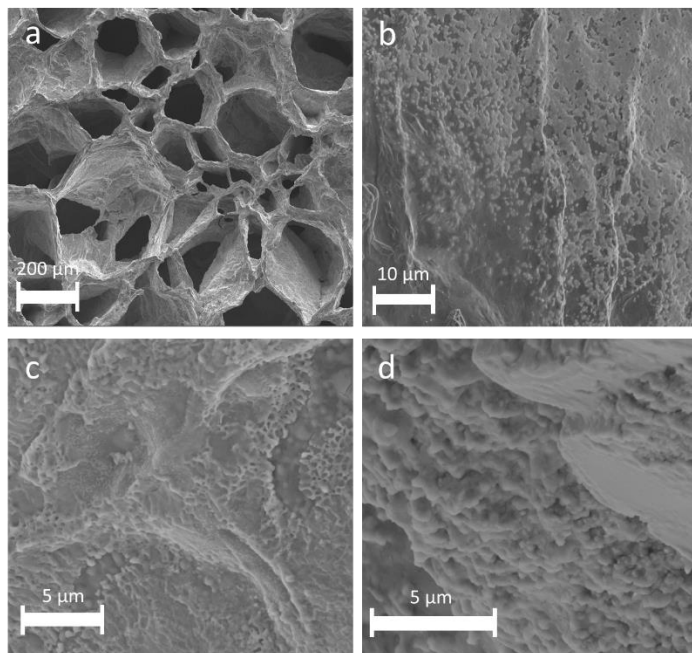


Figure S9. SEM images showing the morphology of LiCl@rGO-SA after 10 times water sorption-desorption cycles in SAWH device. The SEM images show the composite sorbent remains the vertically aligned structures (Figure S9a). Although some LiCl nanoparticles were found again in this sample, we must point out that some LiCl crystals seem agglomerated together. Figure S9b-d show the morphology of LiCl crystals at different locations. We guess this partly crystallization phenomenon is caused by the strong crystallization process during water release process in SAWH device. The more violent crystallization of LiCl solution under fast water release process make the generated crystals have large sizes and irregular shape. However, the thicknesses of salt coatings on the layers of rGO-SA are still very thin to ensure a fast water sorption reaction kinetics.

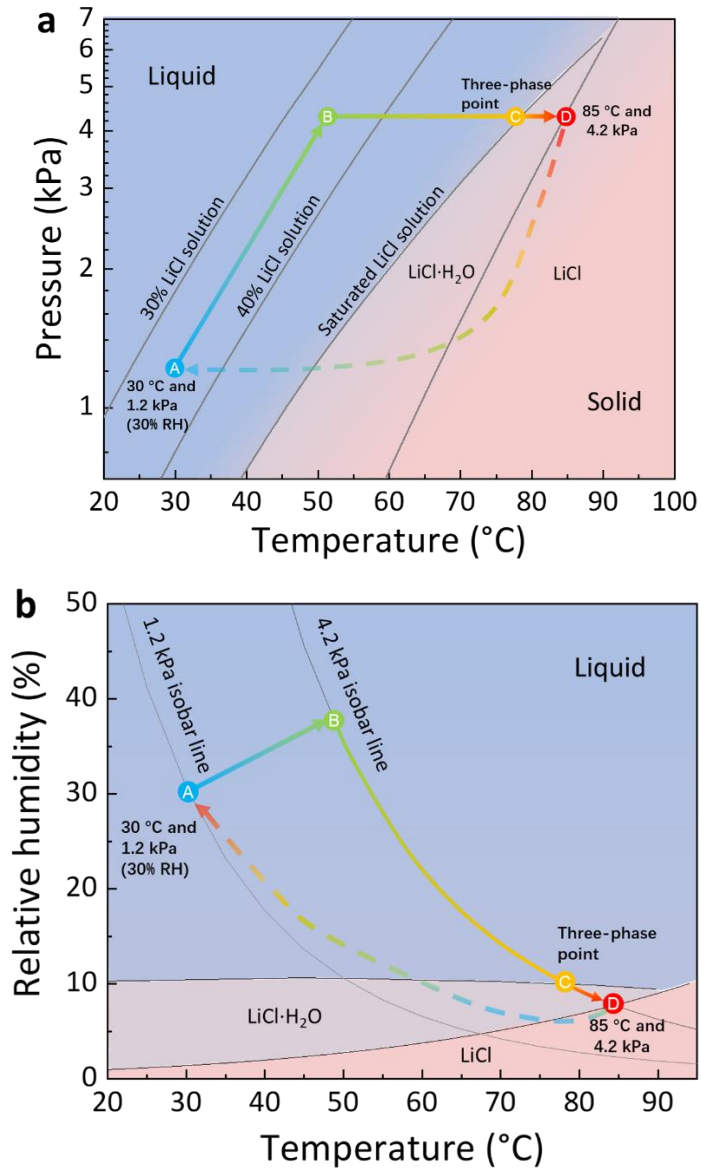


Figure S10. Phase diagram of LiCl-water vapor.¹

(a) Water Pressure-Temperature (P-T) phase diagram. The P-T phase diagram consists of theoretical water sorption equilibrium lines of dilute LiCl solutions, saturated solution, and LiCl¹. A typical SAWH cycle is also given here to show the phase transition during water release (Point A to Point D) and water capture (Point D to point A) process.

(b) Relative Humidity-Temperature (RH-T) phase diagram. Considering the LiCl capture water from ambient air, where relative humidity is more direct than water partial pressure, the RH-T phase diagram marked with the typical SAWH cycle is also provided at here. The RH-T equilibrium verifies the phenomenon of characteristic transition relative pressure of salt deliquescence stays at ~11% RH while that of salt chemisorption has a positive correlation with temperature.

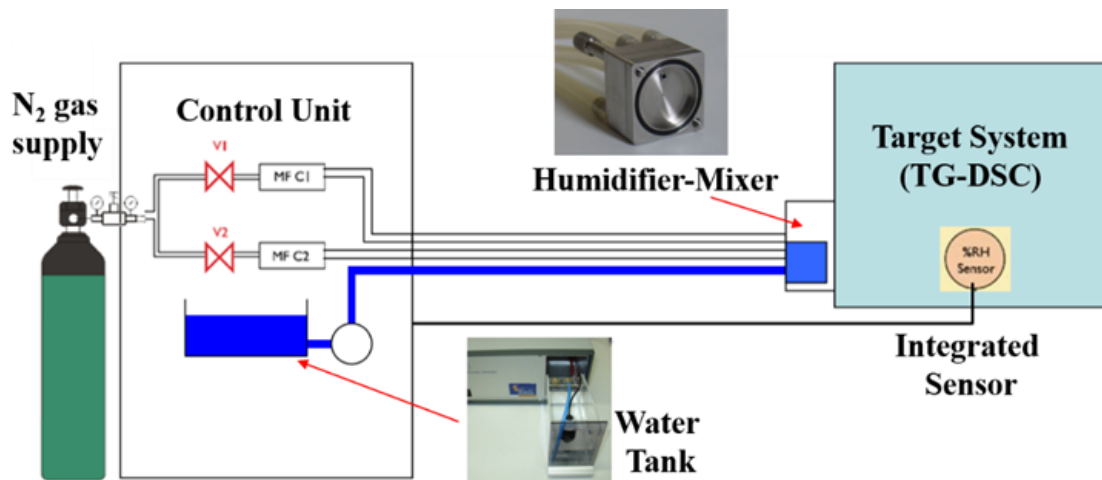


Figure S11. Schematic diagram of the water vapor generating system of thermogravimetric analyzer (STA 449, Netzsch) equipped with a moisture humidity generator (MHG 32, ProUmid)². The water vapor generation system consists of two purge gases of N₂ gas, one flow inside liquid water carrying water vapor (100% RH) and the other one is dry N₂ (0% RH), which mix in a humidifier-mixer. By control the flux of these two purge gases, the humidity of mixture gas can be adjusted between 0% to 100% RH. Benefit from the highly accurate humidity sensor, this system provides a low deviation of water content (g/kg) less than 4%.

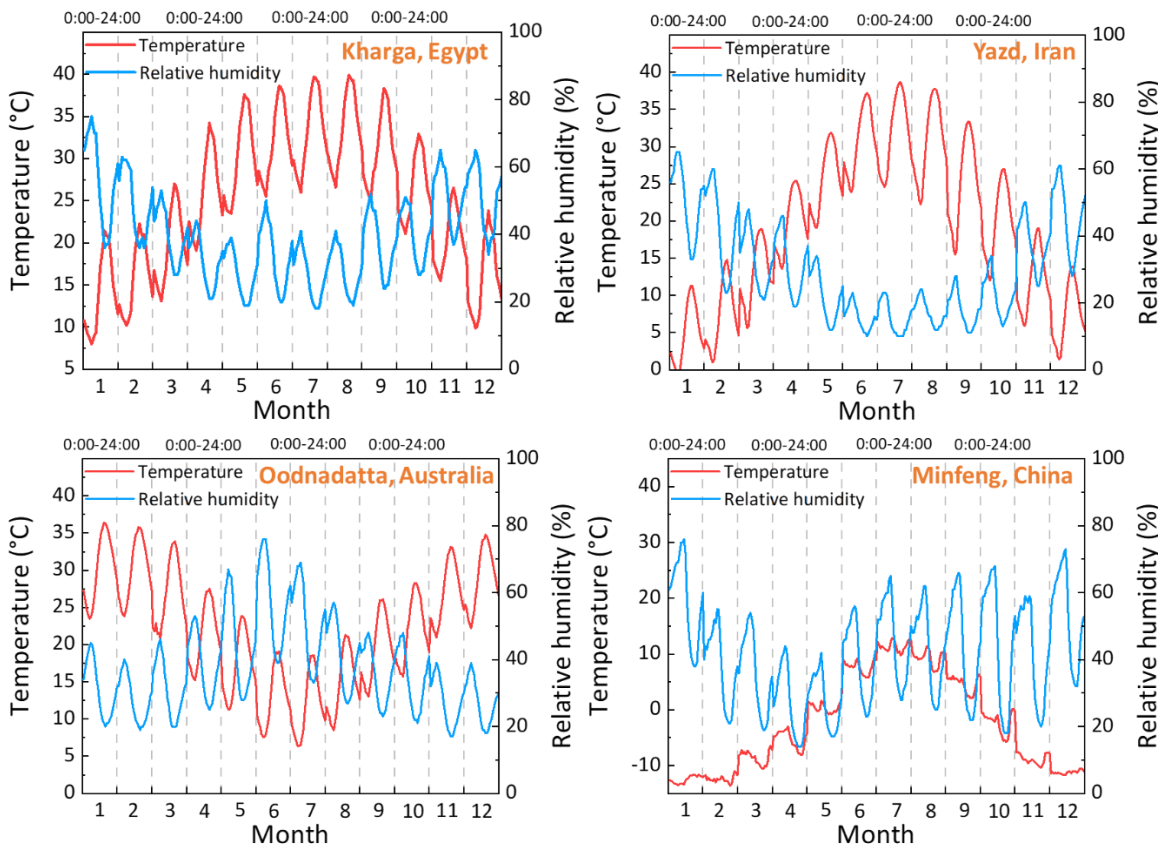


Figure S12. The ambient conditions (Temperature and relative humidity of air) of a typical day in each month at arid regions of Kharga, Yazd, Oodnadatta, and Minfeng³. These four figures show that the daily fluctuations (daytime and nighttime) of T and RH are much stronger than the monthly fluctuation. Especially, even in the summer of the most arid regions, the RH at night was as high as 40% RH, indicating the wide SAWH working conditions ranging 10% -60% RH. Therefore, we carried out the water sorption tests of the nanocomposite sorbent under all of extremely arid (15% RH), semi-arid (30% RH), and moderate (60% RH) conditions in this work.

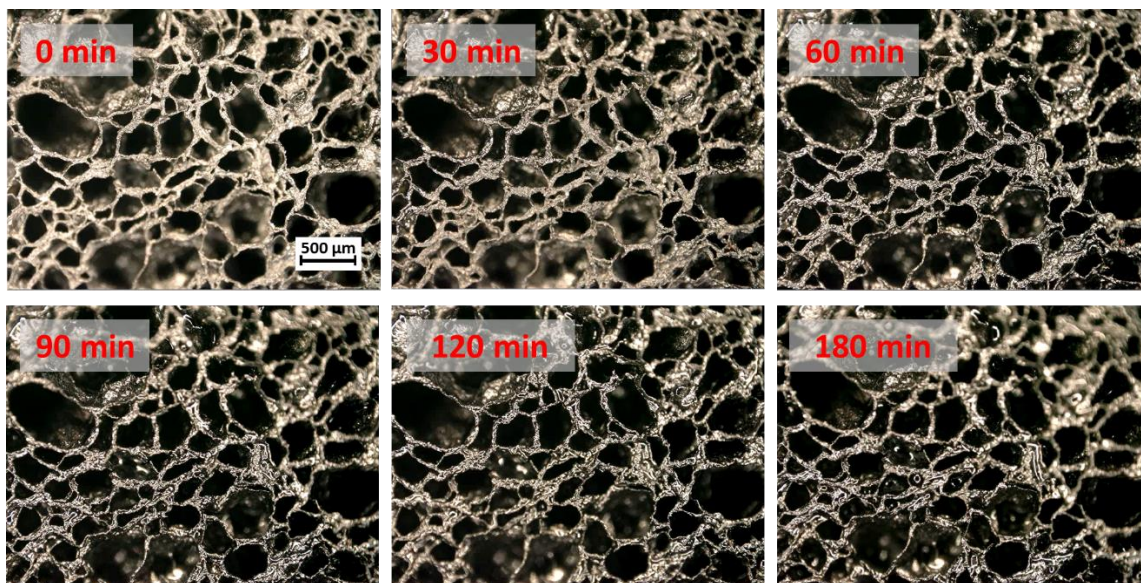


Figure S13. Optical photos showing change of morphology during the water sorption process. The nanocomposite sorbent was exposed in a moisture ambient of $\sim 50\%$ RH, an apparent salt liquefying process was found during water capture process. The liquid salt solution always stays inside pores without leakage, indicating its well stability.

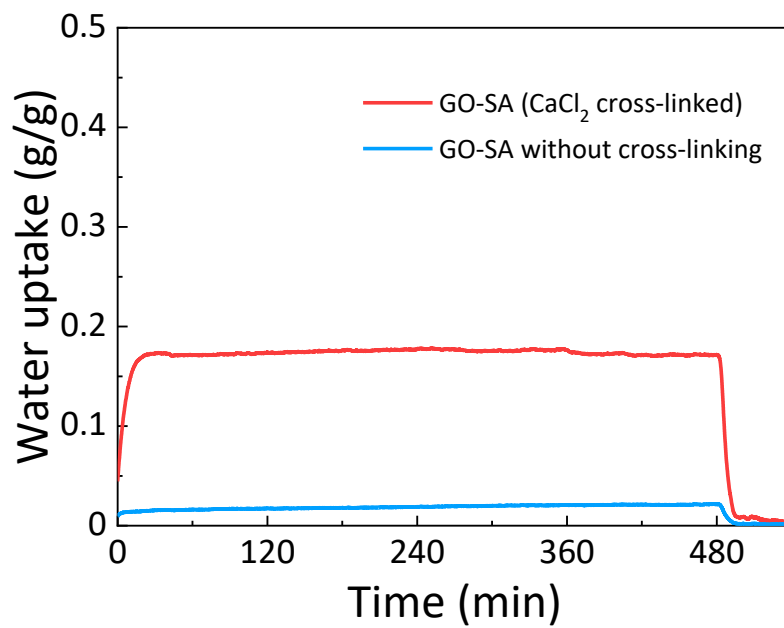


Figure S14. The TGA curves showing the dynamic water sorption process of GO-SA matrixes before and after cross-linking under testing condition of under 30°C, 1.2 kPa (30% RH) for sorption and 90 °C, 4.2 kPa for desorption.

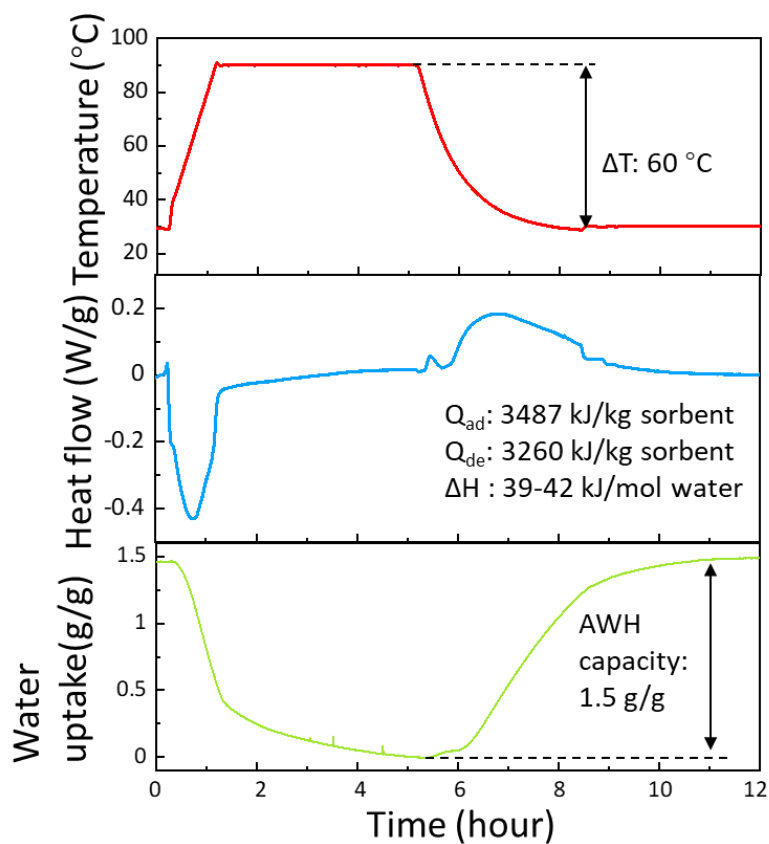


Figure S15. TG-DSC (coupled thermogravimetric and differential scanning calorimetric analysis) curves showing the dynamic water sorption-desorption process of LiCl@rGO-SA under working condition of 30% RH, 30 °C for sorption and 6.0% RH, 90 °C for desorption. By the integrating of heat flow, the heat storage/release density during the water sorption-desorption are determined as 3260 kJ/kg and 3487 kJ/kg sorbent, indicating its high potential for sorption-based heat transformation.

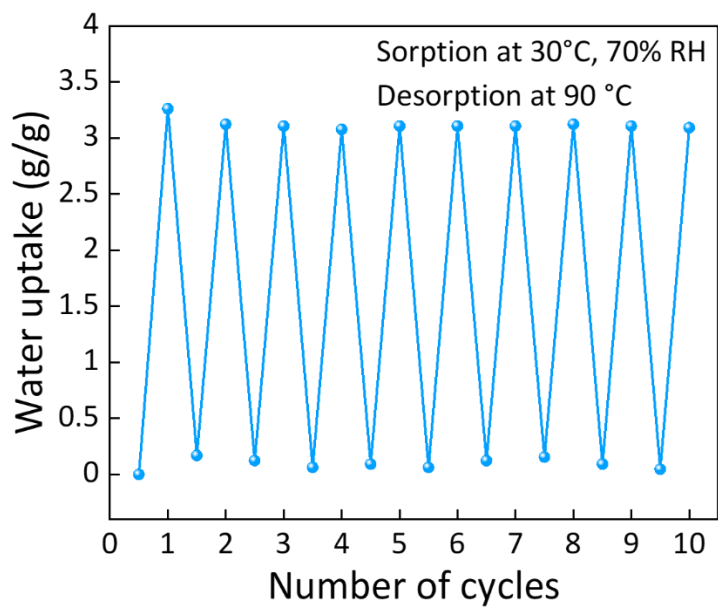


Figure S16. Repeated water sorption-desorption cycling tests of nanocomposite sorbent under 30°C, 70% RH for sorption and 90 °C for desorption.

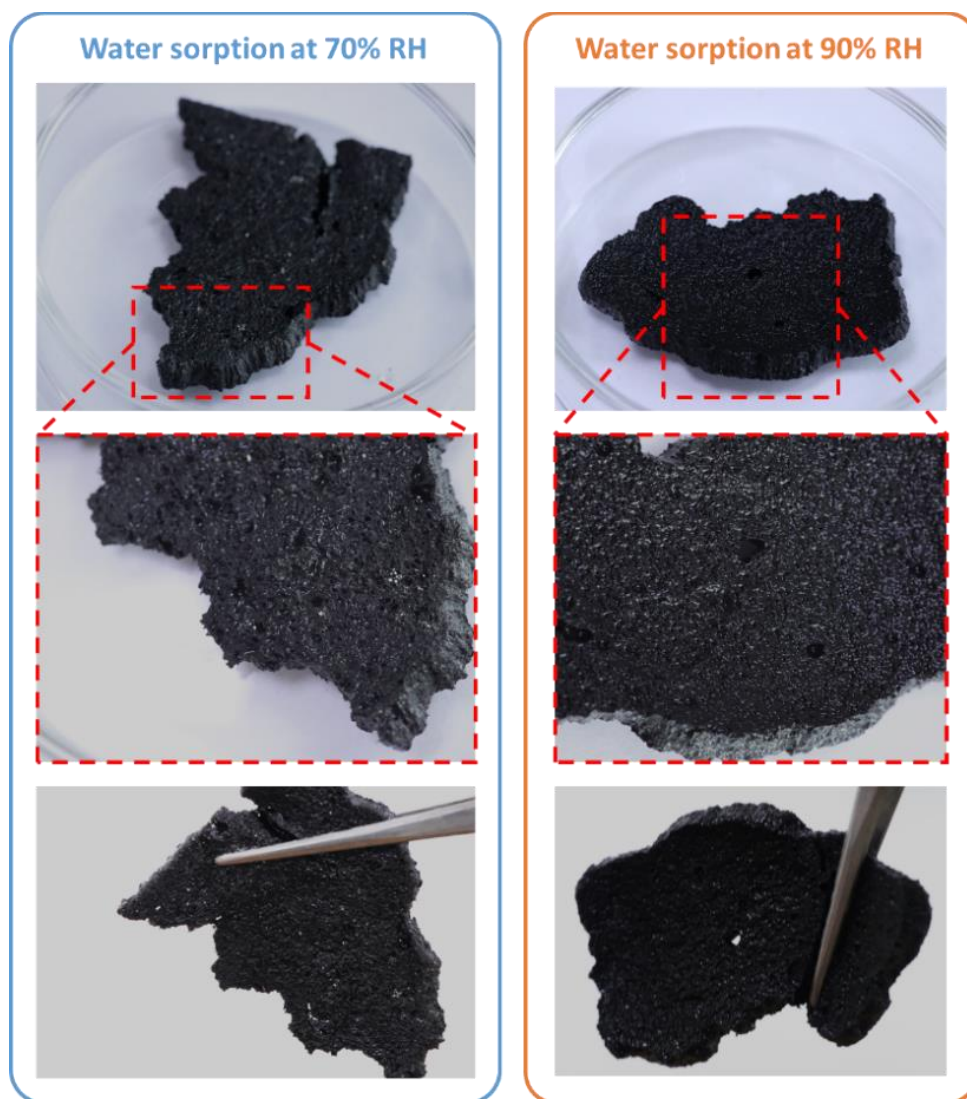


Figure S17. Photos of the nanocomposite sorbent, LiCl@rGO-SA, reaching sorption equilibrium under 30°C, 70% RH and 30°C, 90% RH.



Figure S18. Contact angles of GO, GO-SA, Cross-linked GO-SA, and LiCl@rGO-SA with water droplet. The measured contact angle of GO is close with the reported value of GO, 62.8° , in literature.⁴

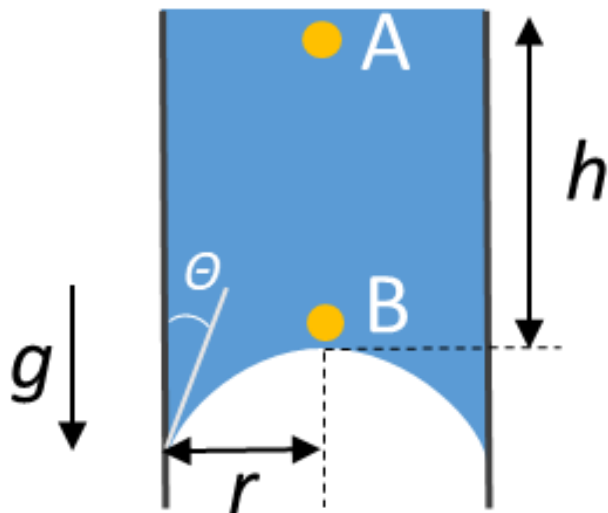


Figure S19. Schematic showing the structure and static force balance of the hanging vertically aligned composite sorbent with captured water.

The captured water reaches a force balance of gravity and capillary force, as shown in Figure S19. The capillary pressure can be described by following well-known Kelvin equation,

$$P_B - P_A = \frac{2\alpha\cos\theta}{r} \quad (\text{S28})$$

where the α is the surface tension at the liquid-gas (solution-air) interface, the θ is the contact angle at the solid-liquid (matrix-solution) interface, and the r is the radius of pores. For pure water and 10wt% LiCl aqueous solution, their surface tensions are 73 mN/m² and 77 mN/m², respectively. Since the capillary pressure are equals to the gravity pressure, ρgh , the height (h) of trapped water column can be expressed by following equation.

$$h = \frac{2\alpha\cos\theta}{\rho gr} \quad (\text{S29})$$

Accordingly, to avoid the dropping out of water, the height of such vertically aligned pores should be controlled in a limited value. In other words, it is desirable to design such sorbents with high hydrophilics (smaller θ) and small pore size (smaller r) to obtain a higher upper limits of height. For this sorbent of LiCl@rGO-SA, its horizontal contact angle with water is about 13.5° (Figure S18) and its pore radius ranges from 2 μm to 100 μm (Figure 1J). If we assume the lowest contact angle is equal to the measured horizontal contact angle, we can roughly estimated the maximum height of trapped water is about 14.5-723 cm, much higher than the selected thickness of sorbent about 3 mm. Therefore, the water can be well trapped in such pores.

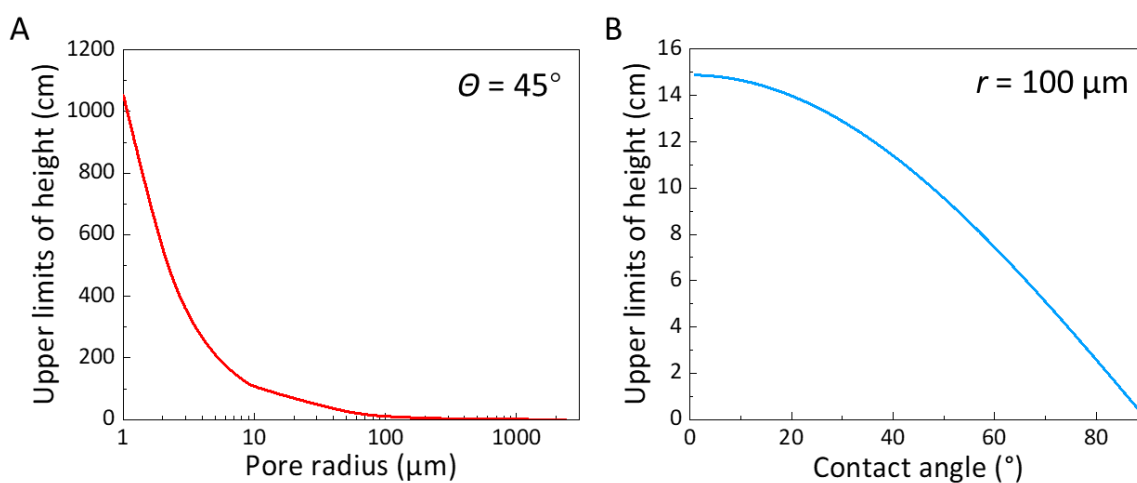


Figure S20. The maximum height of trapped water without leakage for composite sorbent with different pore radius and contact angles. (A) different pore radius and fix contact angle of 45° . (B) different contact angles and fixed pore radius of $100 \mu\text{m}$. Considering above results are obtained according to the above static force analysis, the upper limited height may be much lower for practical applications under vibration conditions. Therefore, it is suggested to keep a small pore radius less than $100 \mu\text{m}$ and a low the contact angle less than 30° for ensuring a high durability.

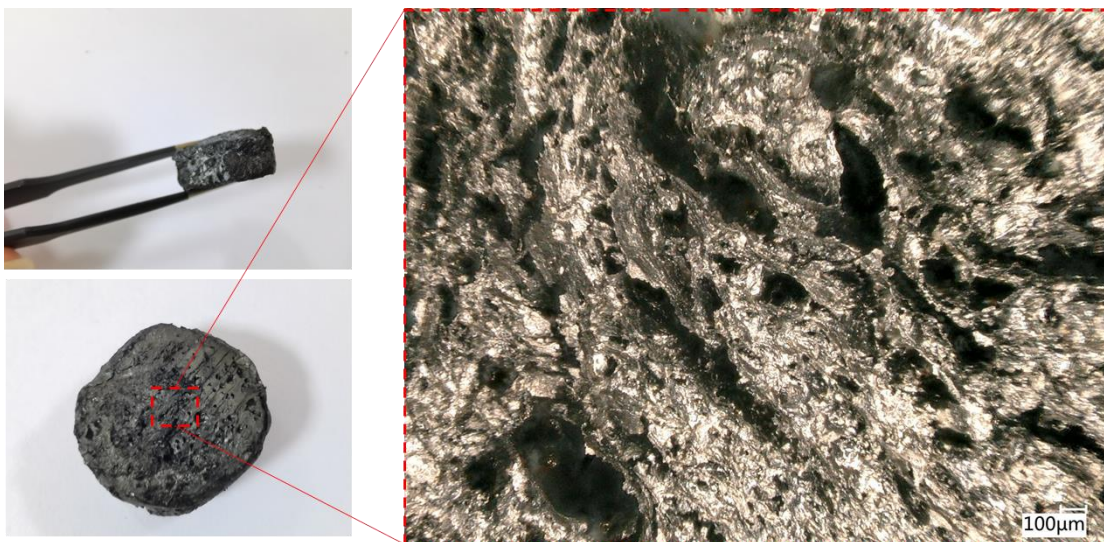


Figure S21. The optical images showing the pore structures of LiCl@rGO-SA_unordered. This composite sorbent was synthesized using nondirectional method with a uniform freezing process, named as LiCl@rGO-SA_unordered. This composite sorbent was used for comparing the sorption kinetics with vertical aligned LiCl@rGO-SA to uncovering the contribution of vertical aligned pores on improving sorption kinetics.

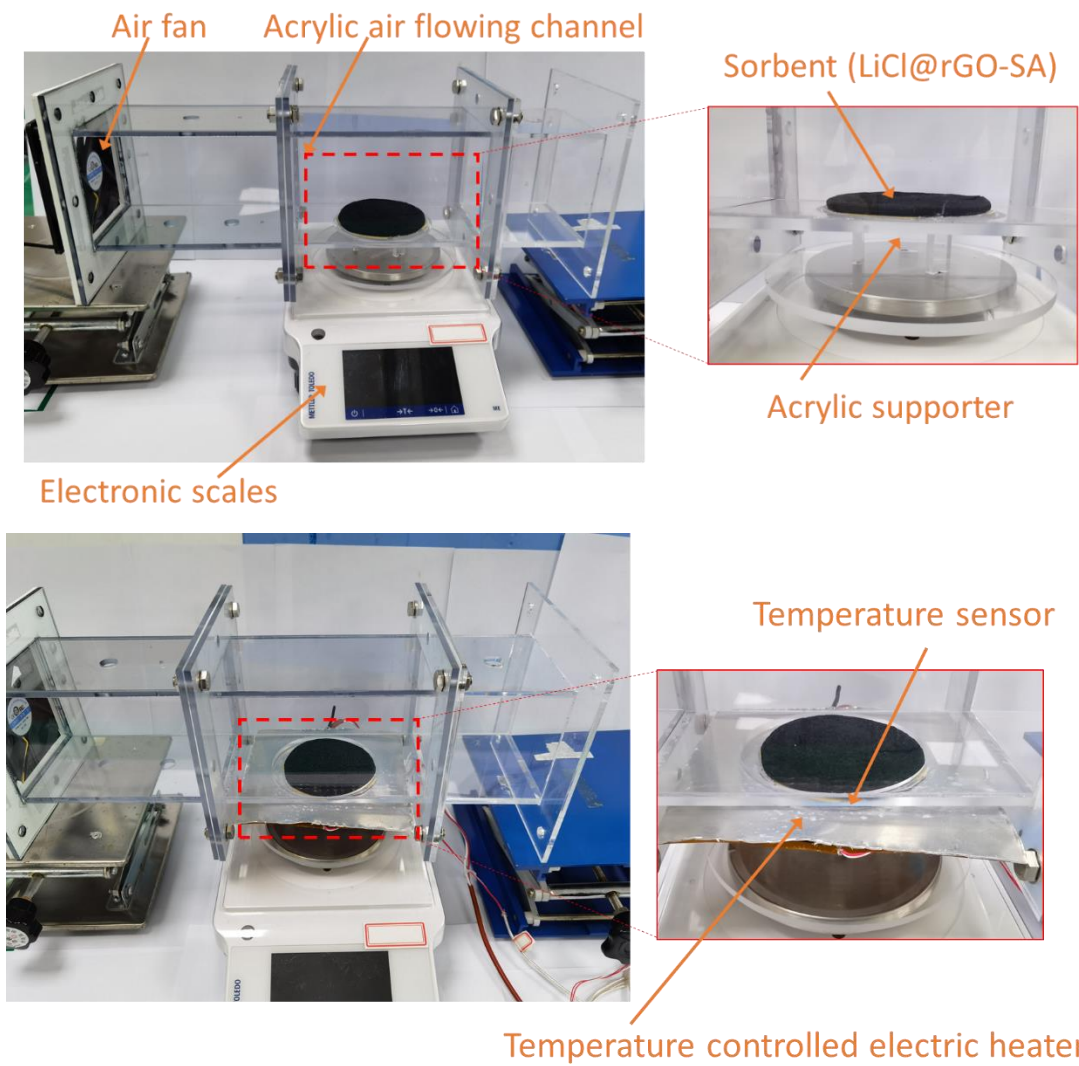


Figure S22. Optical photo of the water sorption-desorption kinetics testing device (Top photo of sorption, bottom photo of desorption). A temperature-controlled electric heater is used to driving the water desorption at a constant temperature.

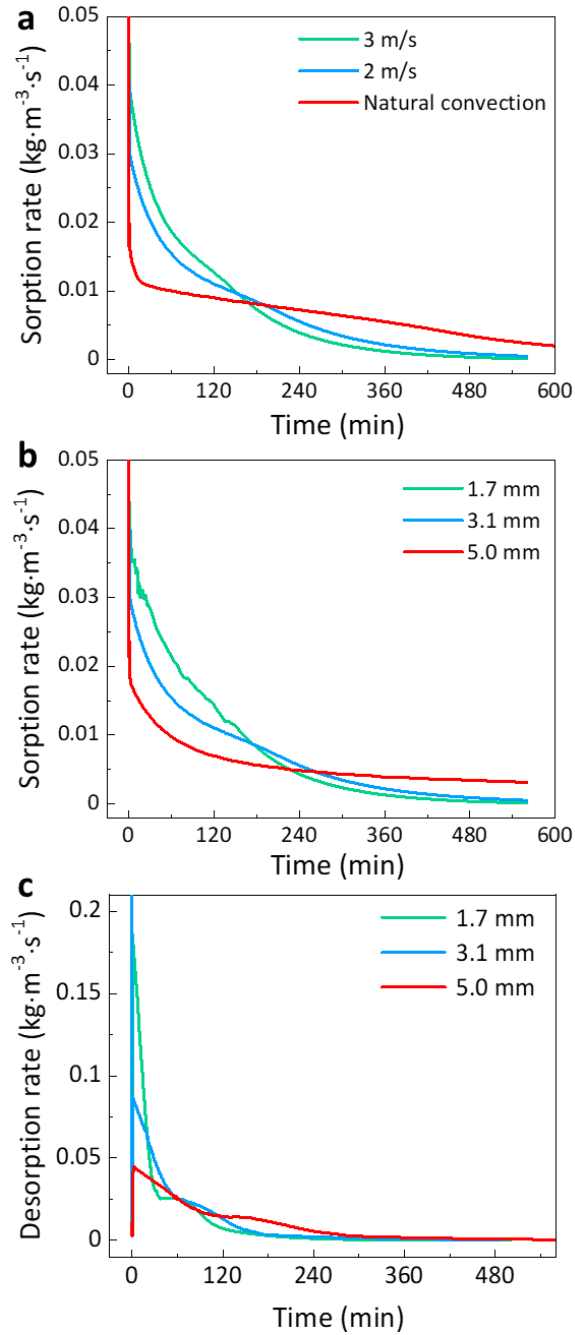


Figure S23. The simulated adsorption/desorption rates evolutions for different cases.

(a) The water sorption rate of sorbents with thickness of 3.1 mm under different convection conditions.

(b) The water sorption rates of sorbents with different thicknesses under 30% RH with an air flow rate of 2.0 m/s.

(c) The water desorption rates of sorbents with different thicknesses after reaching water sorption equilibrium under 30% RH.

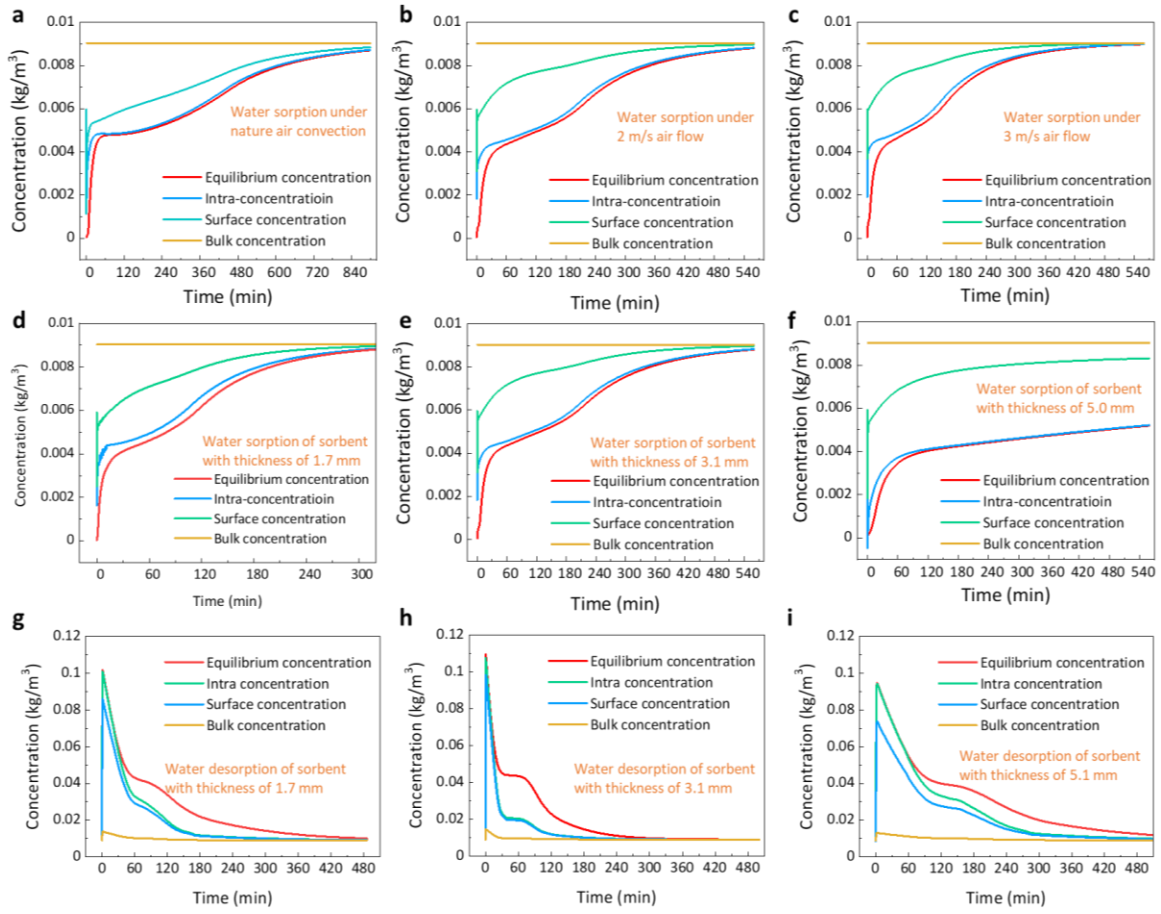


Figure S24. The simulated water vapor concentrations evolutions of bulk concentration (C_{amb}), surface concentration (C_{surf}), intra-concentration (C_{sorb}), and equilibrium concentration ($C_{sorb,eq}$) during water sorption-desorption process.

(a-c) Water sorption at 30% RH for LiCl@GO-SA with thickness of 3.1 mm under different convection condition without convection, with air flow of 2.0 m/s, and with air flow of 3.0 m/s.

(d-f) Water sorption at 30% RH with air flow rate of 2.0 m/s for LiCl@GO-SA with thicknesses of 1.7 mm, 3.1 mm, and 5.0 mm.

(g-i) Water desorption after sorbent reaching sorption equilibrium at 30% RH with natural air convection for LiCl@GO-SA with thicknesses of 1.7 mm, 3.1 mm, and 5.0 mm.

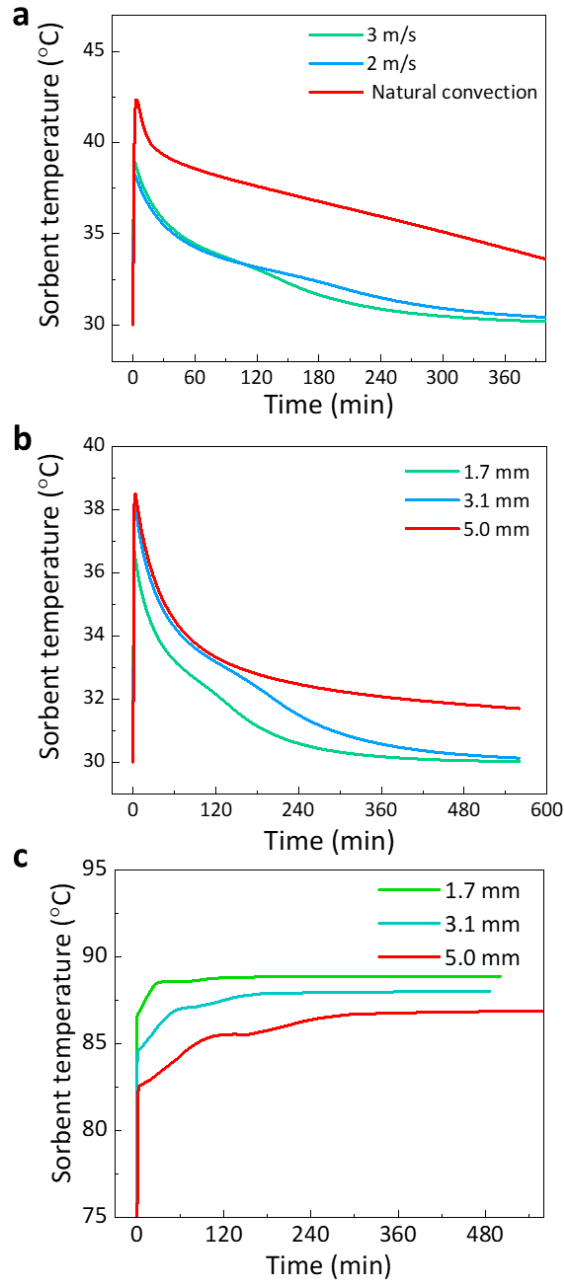


Figure S25. The simulated evolutions of sorbent temperatures during water sorption-desorption process.

(a) The temperatures of sorbents with thickness of 3.1 mm under different convection conditions during water sorption process.

(b) The temperatures of sorbents with different thicknesses under 30% RH with an air flow rate of 2.0 m/s during water sorption process.

(c) The temperatures of sorbents with different thicknesses during water desorption process after saturated under 30% RH.

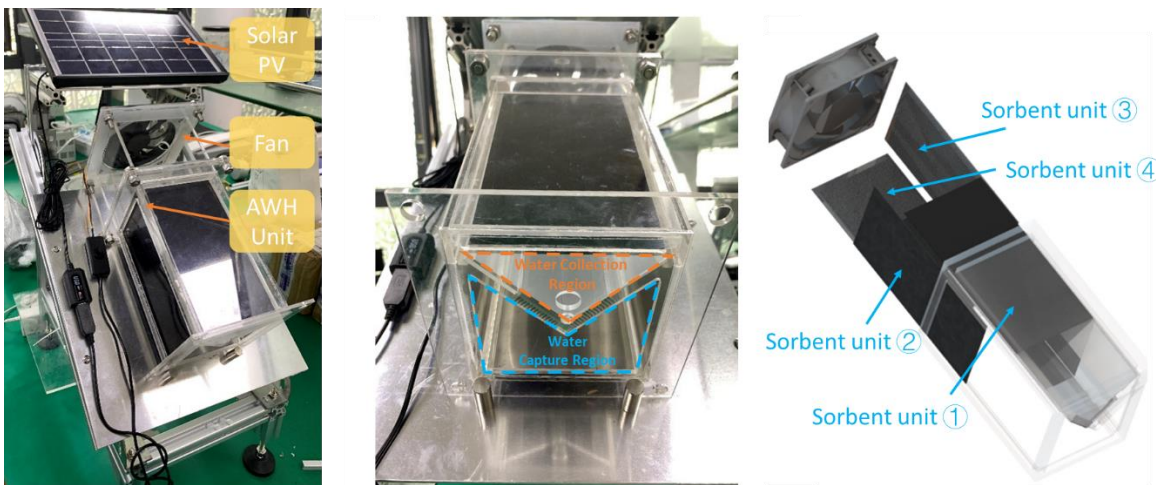


Figure S26. Structures of the compact semi-active SAWH device. The device was put on an inclined plane with an angle of 30° for the perpendicular light shining on sorbent bed.

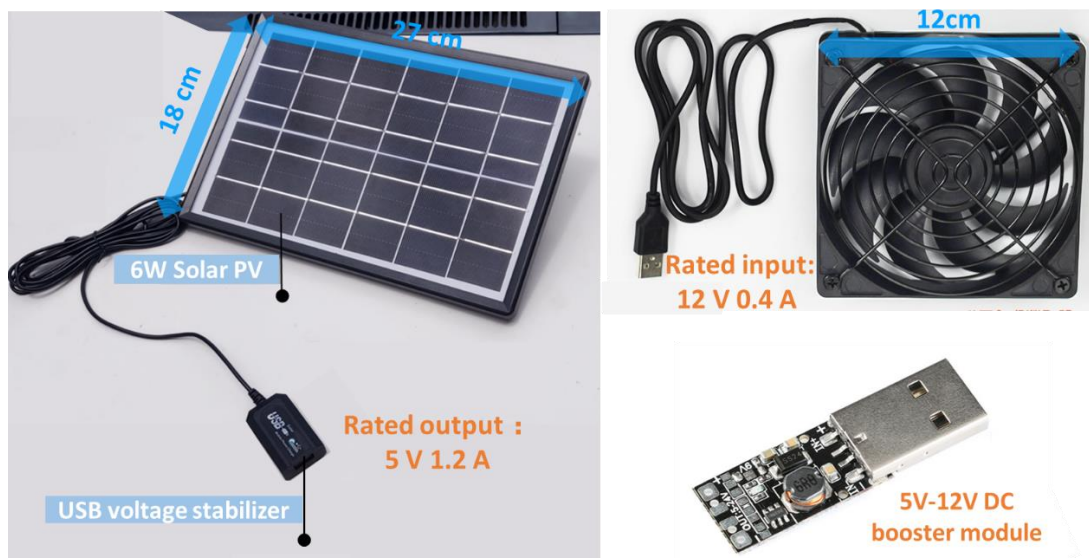


Figure S27. The photos of PV panel and the air fan. We selected an 18*27 cm commercial PV panel (weight, 564 g) to generate a 6 W output. A USB voltage stabilizer was used to control the output voltage at a stable value of 5 V. To realize a high speed of air flow rate, a 12 V powered air fan was used in this device. Therefore, a 5 V-12 V DC booster was used to match the output of solar PV panel and the input of air fan.

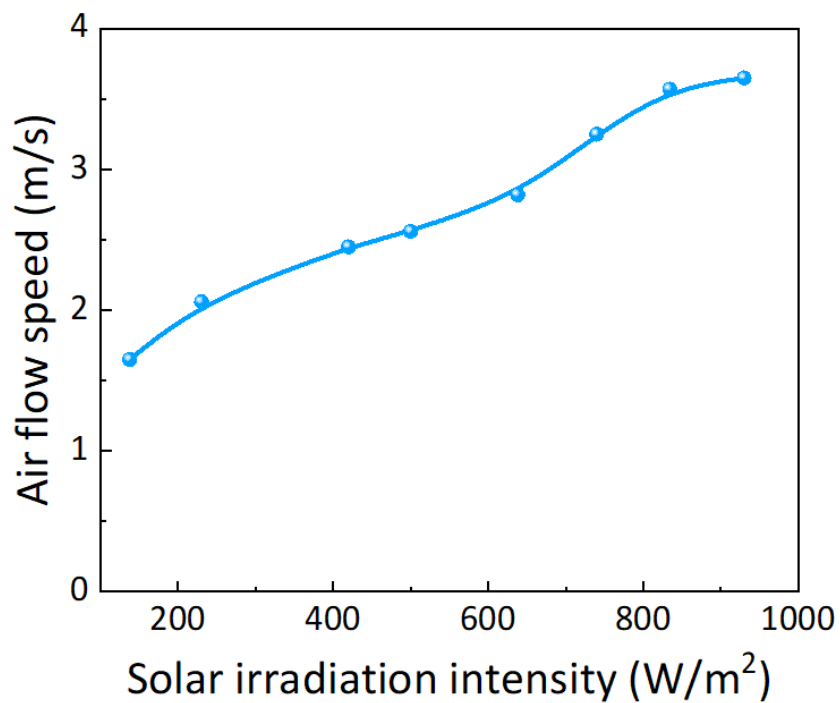


Figure S28. The air flow speeds in the SAWH device under different solar irradiation intensities. As can be seen, the solar-powered fan can be driven even at a cloudy day with a low solar irradiation intensity below 200 W/m².

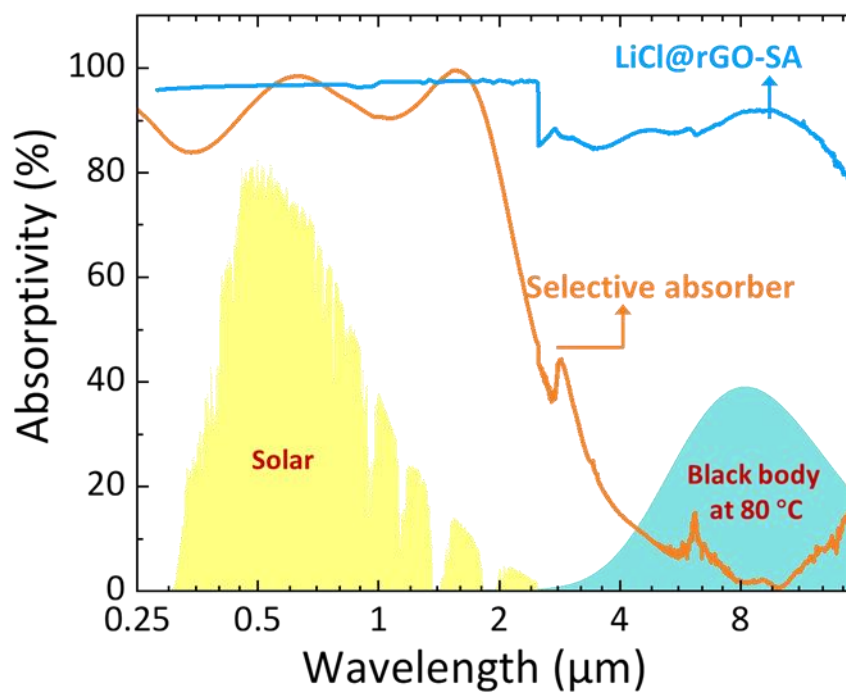


Figure S29. The light absorbance of LiCl@rGO-SA and commercial selective solar absorber over a wide spectrum range from 250 nm to 15 μm.

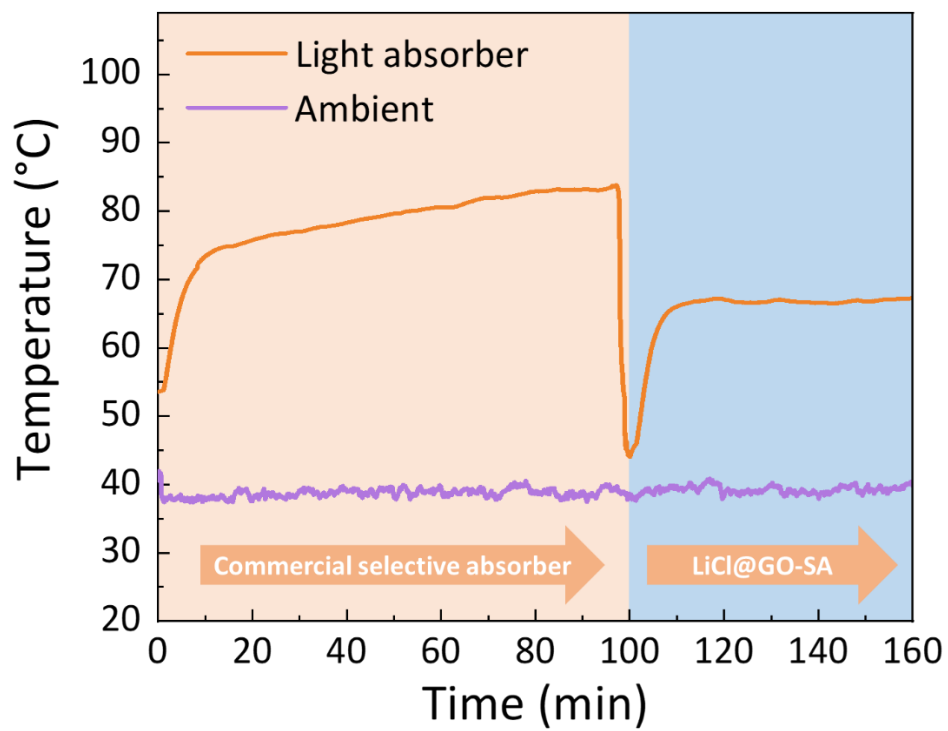


Figure S30. The solar collection temperatures of commercial selective absorber and LiCl@GO-SA under a natural solar irradiation of 900-1000 W/m².

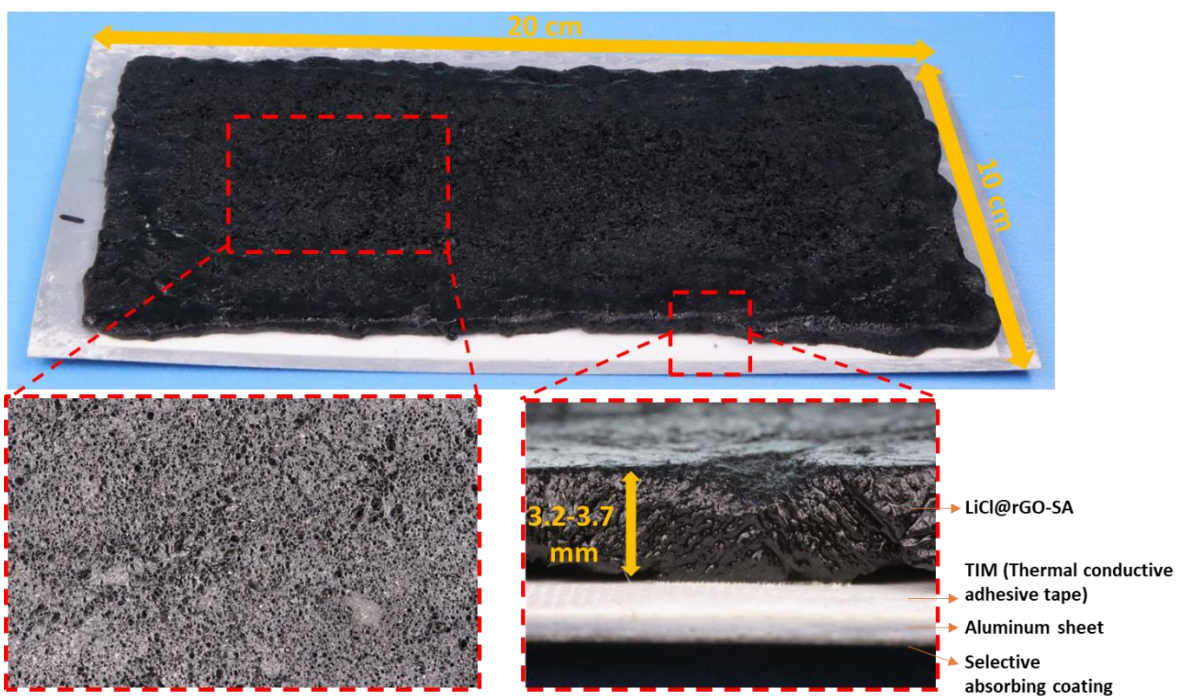


Figure S31. The photos of the sorbent unit. The nanocomposite sorbent of LiCl@rGO-SA is directly stucked on back side of selective solar absorber (the selective absorbing coating on the aluminum sheet).

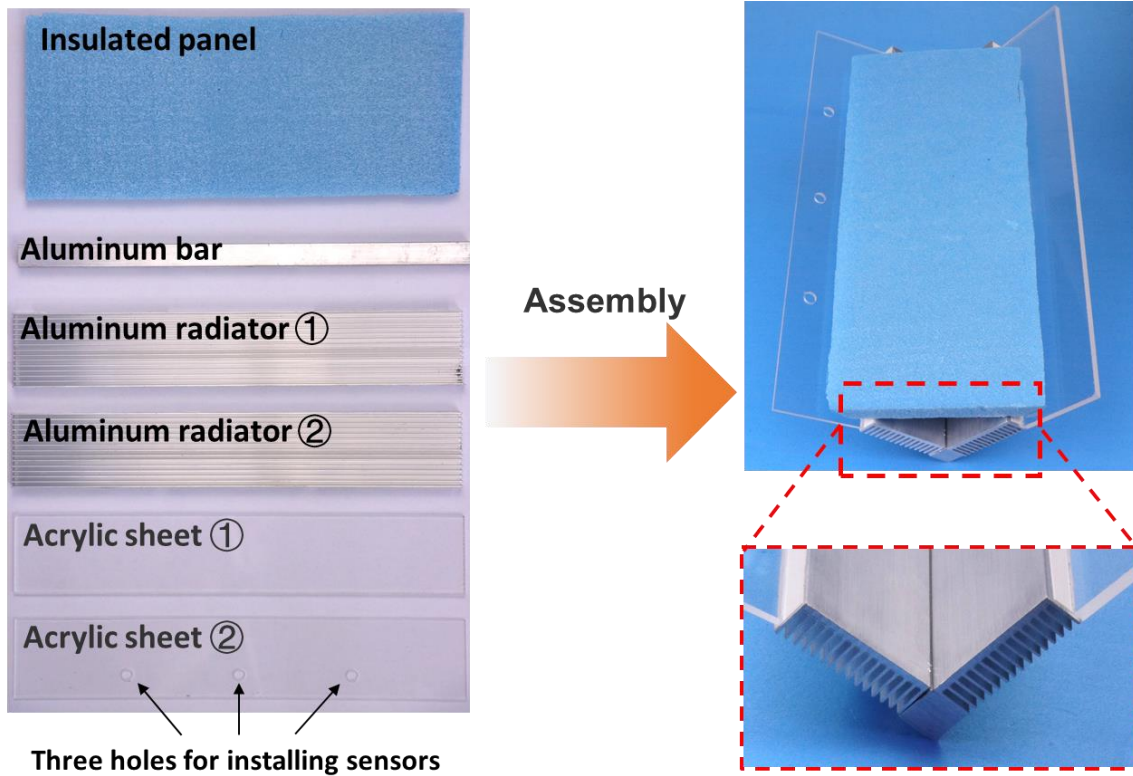


Figure S32. Structure illustration of the compact water condenser.

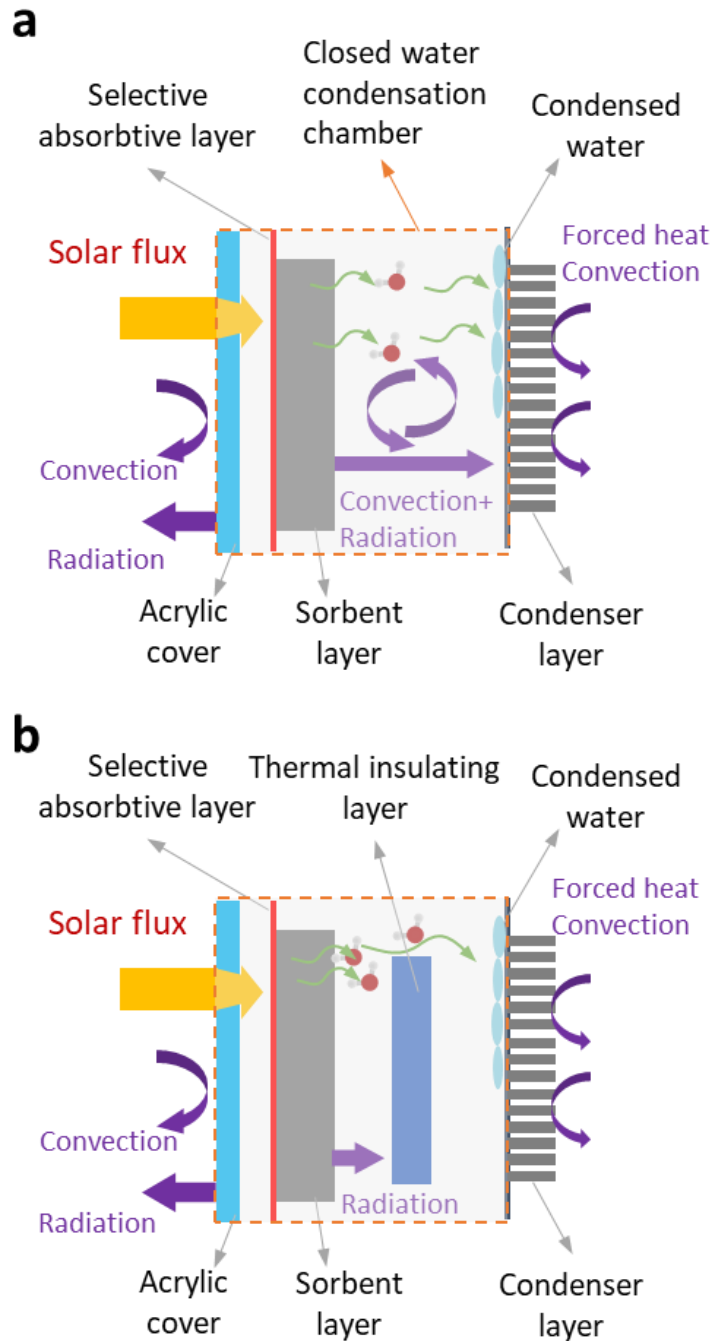


Figure S33. Thermal analysis of the water desorption-condensation process for the compact SAWH device.

(a) without insulation panel.

(b) with insulation panel between adsorbent and condenser.

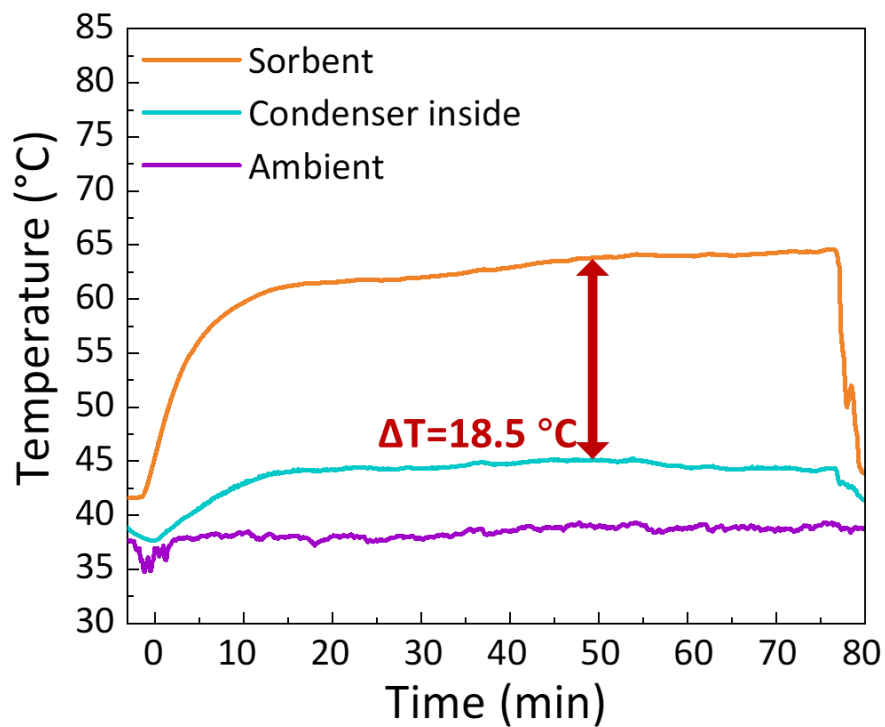


Figure S34. The temperature evolutions of sorbent, condenser, and ambient air for the SAWH without installing an insulated panel between sorbent and condenser under a stable solar irradiation of 950 W m^{-2} .

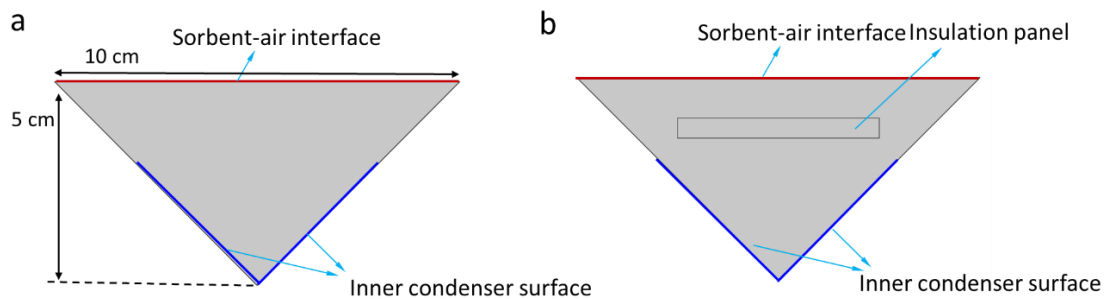


Figure S35 a. The geometric construction of device without insulating panel. b. The geometric construction of device with insulating panel.

Three cases with different structures were studied via COMSOL, corresponding to the different mass transfer conditions of without insulation panel, with impermeable insulation panel, and with permeable insulation panel (permeability, 10^{-12} m^2) respectively. The space between insulation panel and acrylic enclosure is set at 10 mm. The simulation is calculated under simplified boundary conditions of fixed condensation and desorption temperatures for the first two cases without insulation panel and with impermeable insulation panel, whose detailed data refers to the measured results in Figure 4D. For the device with permeable insulation panel, its boundary conditions are set as the same condensation temperature and same mass flux (J) with that of case using impermeable insulation panel. As shown in following Figure S38, since the insulation panel apparently reduce the air convection velocity near the sorbent, bringing a higher heating temperature, the estimated diffusion flux with the insulating panel is about 24% higher than the diffusion flux without insulating panel.

In comparison with the impermeable insulating panel, the permeable insulating panel can effectively decrease of mass resistance, which means it provides same water transport rate (J) under a lower vapor pressure difference ($P_{\text{vapor, sorbent}} - P_{\text{vapor, cond}}$) condition. We estimated the vapor pressure difference with permeable insulating panel as about 6.5 kPa compared to 10.5 kPa for the case using the impermeable insulating panel, accompanying with a lower required desorption temperature decreasing about 5.4 °C.

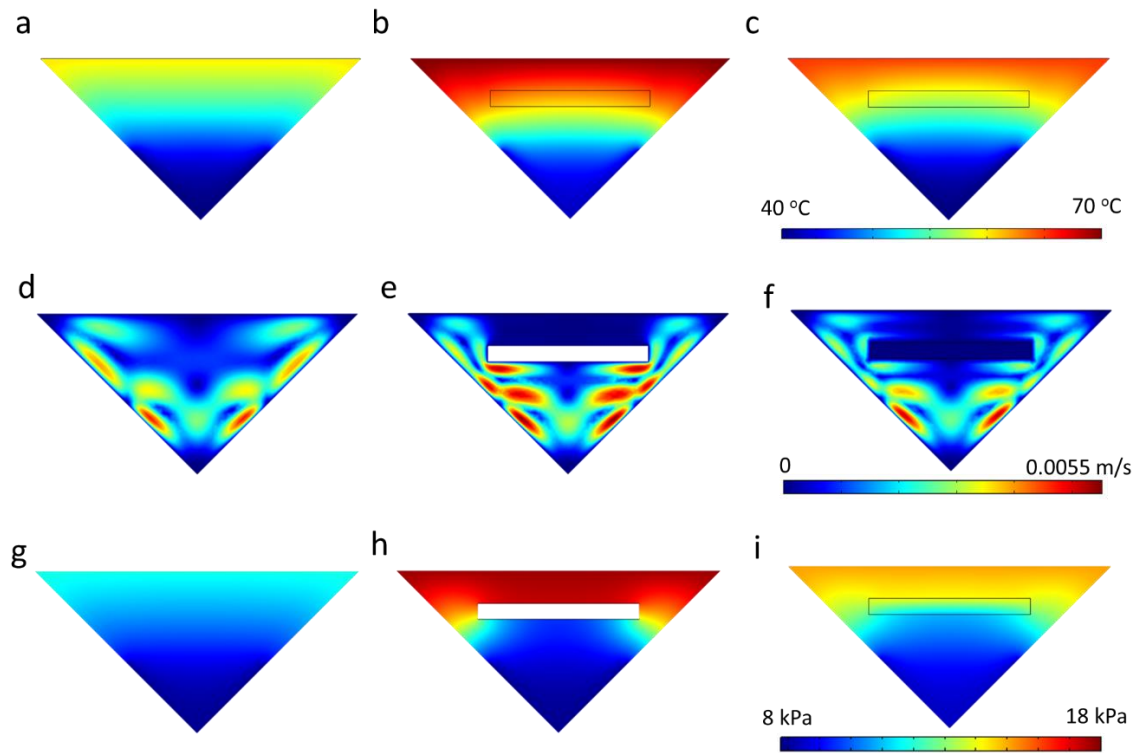


Figure S36. The simulation results of water release-condensation process. The temperature distributions in devices without insulating panel structure (a), with impermeable insulating panel structure (b), and with permeable insulating panel structure (c). The velocity distributions in devices without insulating panel structure (d), with impermeable insulating panel structure (e), and with permeable insulating panel structure (f). The concentration distributions in devices without insulating panel structure (g), with impermeable insulating panel structure (h), and with permeable insulating panel structure (i).

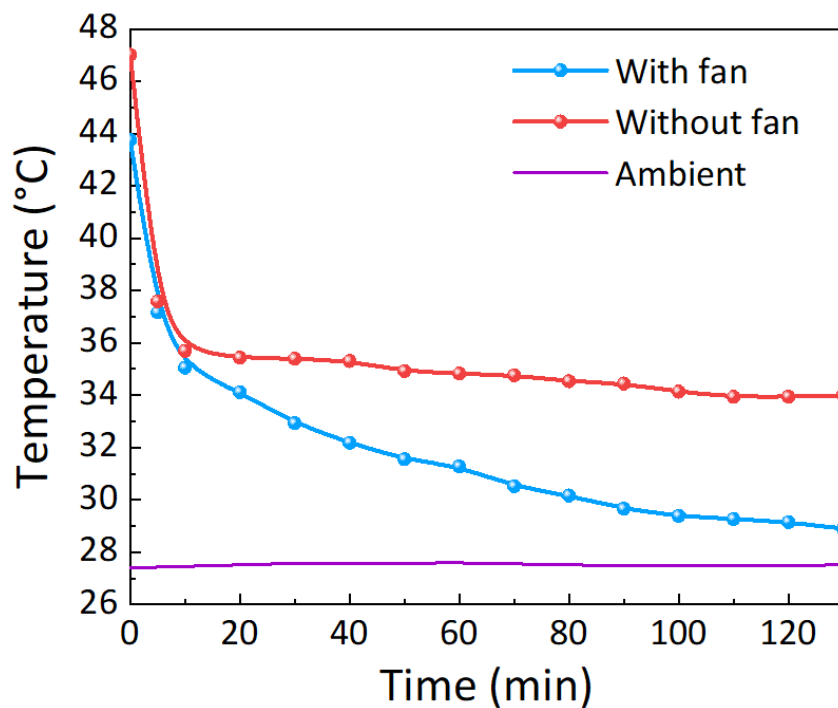


Figure S37. The evolutions of sample temperatures at center points (data extracted from infrared temperature mapping). With the assistance of fan-driven forced air low, the sorbent temperature can fast reduce from desorption temperature to near ambient temperature within two hours.

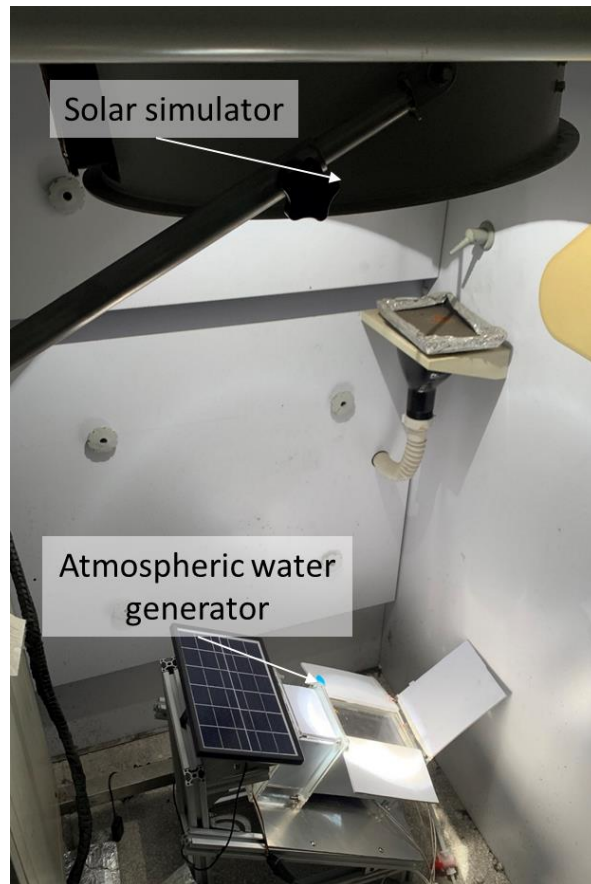


Figure S38. Photo of SAWH testing under laboratory condition (0.95-1.05 kW/m² solar irradiation). The tests were carried out in laboratory under artificial lighting generated by a solar simulator with irradiation intensity of 950-1050 W m⁻² (TRM-PD, Jinzhou Sunshine Technology, spot diameter of 0.2 m), with uniformity of 10 %, temporal instability of 10 %, and spectral match classification of Class B.

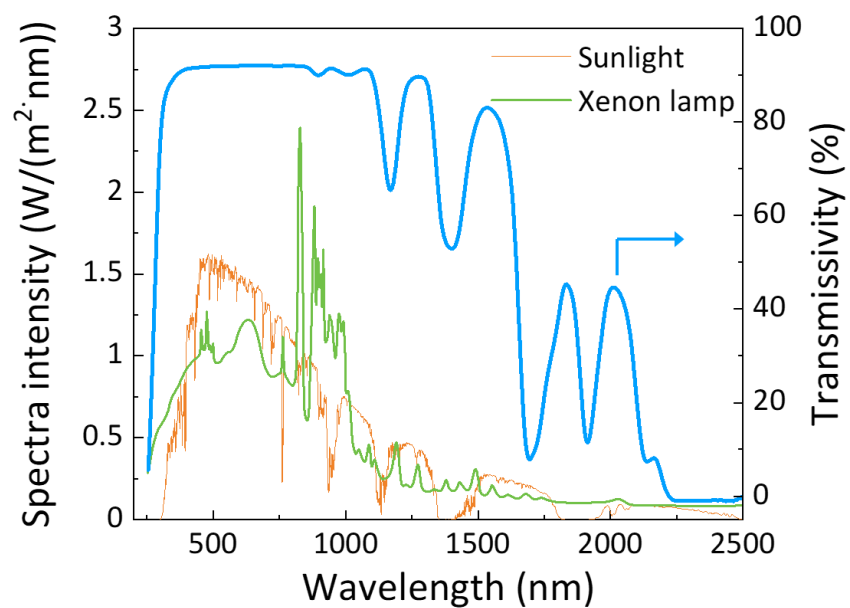


Figure S39. The spectra of sunlight and xenon lamp, and the transmissivity of the acrylic cover. The spectra of xenon lamp is the theoretical curve provided by the producer of solar simulator, Jinzhou Sunshine Technology.

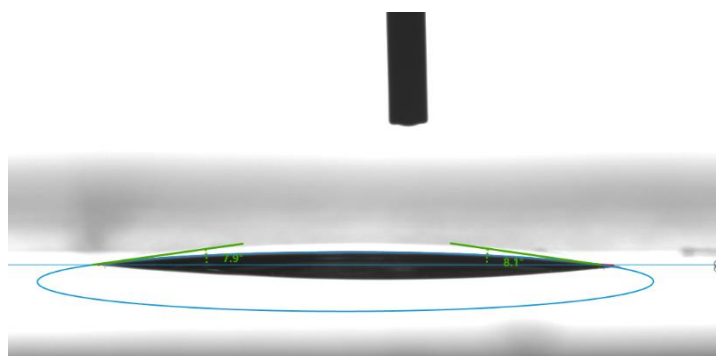


Figure S40. The contact angle of hydrophilic PET membrane with a water droplet.

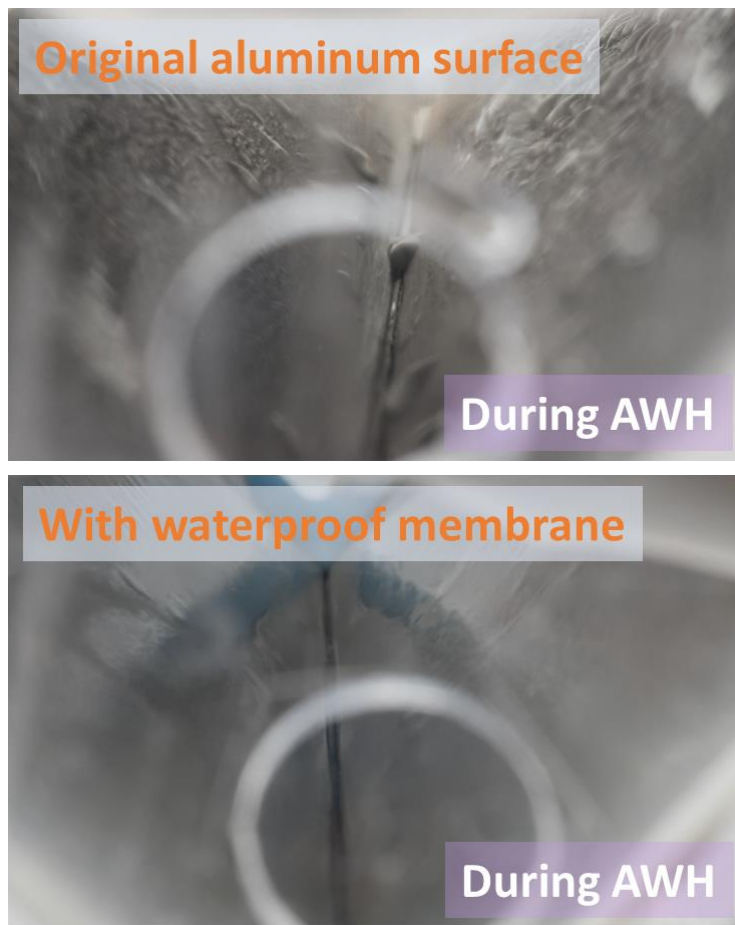


Figure S41. Photos of condensation surface with/without waterproof membrane during water harvesting process. Many of water droplets stays at the surface of the original aluminum, while the aluminum coated with waterproof membrane always keep clean and bright during water condensation process (See dynamic water dropping process in Supplementary Video 2 and Supplementary Video 3).

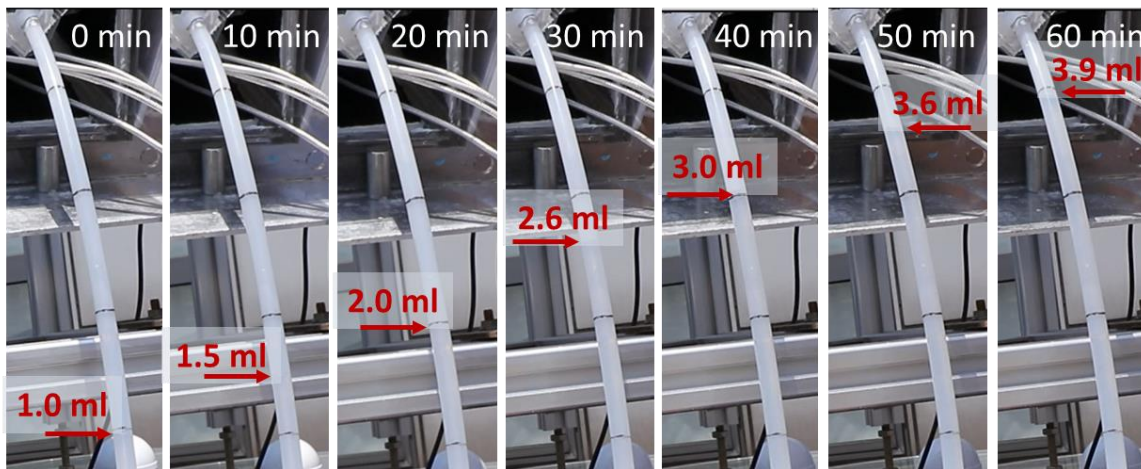


Figure S42. The changes of liquid level of collected water in the silicone tube showing the volume changes of collected water during a typical outdoor water collection cycle. After open the water valve, the harvested water can be easily collected at the end of each cycle.

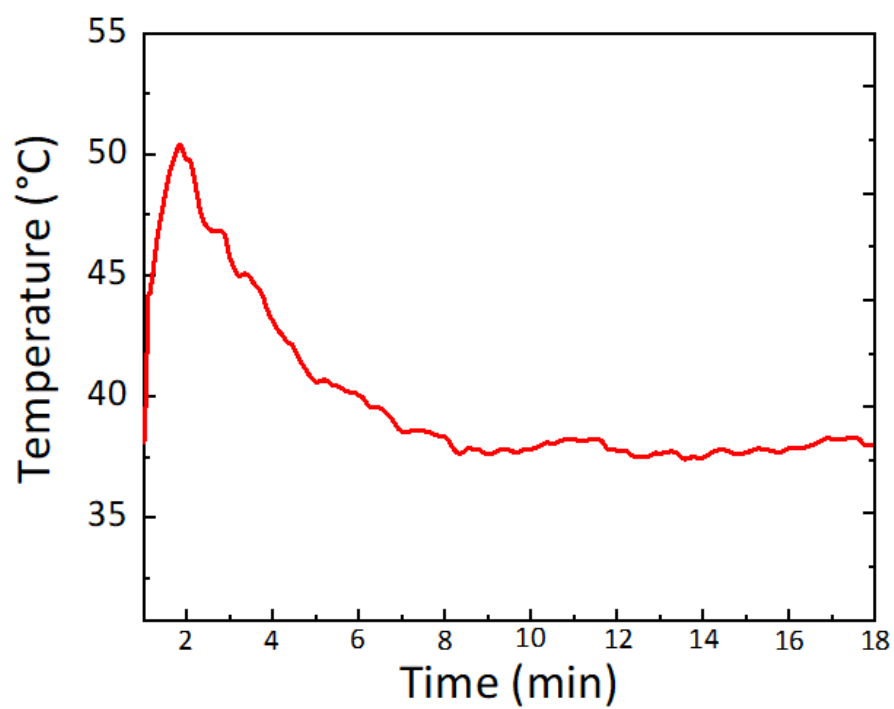


Figure S43. Temperature evolution of the water-released sorbent during its initial phase of air cooling and water sorption.

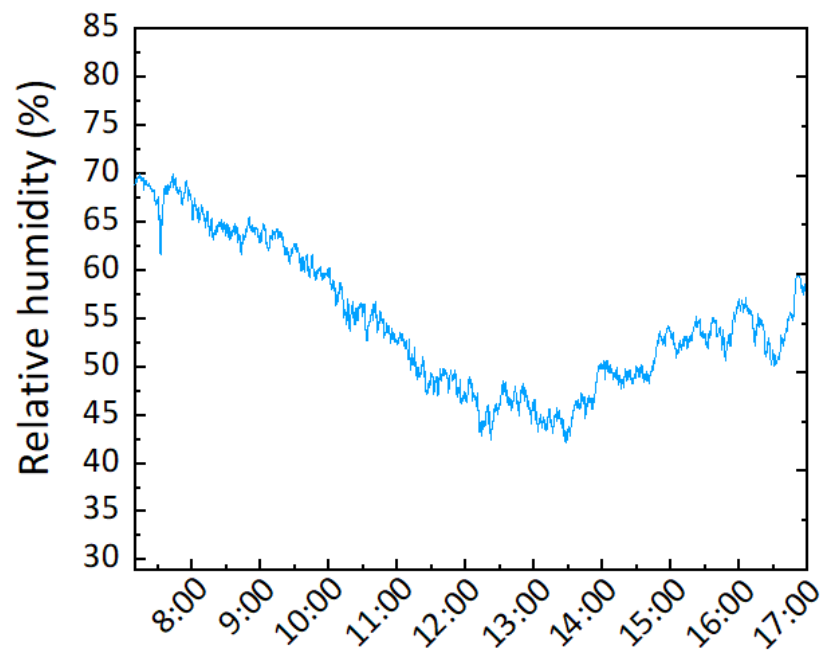
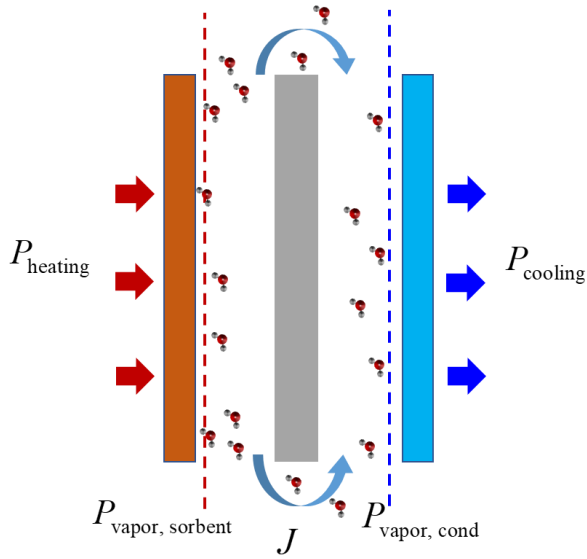


Figure S44. The changes of relative humidity of local ambient air on August 17, 2020. A lowest RH of 42% RH is found at the midday and a highest RH of 70% is found at the morning as result of the temperature changes of ambient air.



Water desorption rate \dot{m}_d :

$$\dot{m}_d = \frac{P_{\text{heating}} \cdot S_d}{\Delta h_d} \quad P_{\text{heating}} = \eta \cdot P_{\text{solar}}$$

Water vapor transport rate J :

$$J = \frac{\Delta P}{R_{\text{total}}} = \frac{P_{\text{vapor, sorbent}} - P_{\text{vapor, cond}}}{R_{\text{total}}} \quad \begin{matrix} P_{\text{sorb}} = P_{\text{eq}}(T_{\text{sorb}}, q) \\ P_{\text{cond}} = P_{\text{sat}}(T_{\text{cond}}) \end{matrix}$$

Water condensation rate \dot{m}_c :

$$\dot{m}_c = \frac{P_{\text{cooling}} \cdot S_c}{\Delta h_c} \quad P_{\text{cooling}} = k \cdot (T_c - T_a)$$

For a stable water collection process:

$$\dot{m}_d = J = \dot{m}_c$$

Figure S45. The mass transport balance during desorption-condensation process for the compact SAWH device.

The water collection process consists of three steps of the water release from sorbent, the water vapor transport from sorbent to condenser, and the water condensation on the surface of condenser; thus, the water collection rates not only related with desorption rates but co-determined by following three factors: i) the water desorption rate (\dot{m}_d , g/s) released from the sorbent driven by the solar heating power (P_{heating} , W/m²), which is determined by the input solar radiative intensity (P_{solar} , W/m²) and the thermal efficiency (η). ii) mass transport rate (J , g/s) from the sorbent to the condenser via molecular diffusion and natural convective transfer, which is determined by the vapor pressure difference ($P_{\text{sorbent}} - P_{\text{cond}}$, g/m³) and the mass transfer resistance (R_{total} , s), wherein the R_{total} the interior structure and the permeability. iii) Water condensation rate (\dot{m}_c , g/s) collected at the condenser driven by the cooling power (P_{cooling} , W/m²), which is determined by the temperature difference and structure of condenser. Since these three steps are in series, these three rates should be equal in a steady water collection process.

According to above analysis, it can be concluded that the apparent water collection rate is controlled by the step which shows the largest resistance. For example, if the heating power is insufficient than the cooling power and the mass transfer rates, the collection rates will be controlled by the heating power, thus the improvement of cooling power and inducing mass transfer resistance are unnecessary in this case. In this study, since the condensation temperature is apparently higher than the ambient temperature, caused by the small condensation surface area, it can be estimated that the major resistance limiting water collection rates comes from the condensation rates rather than the others.

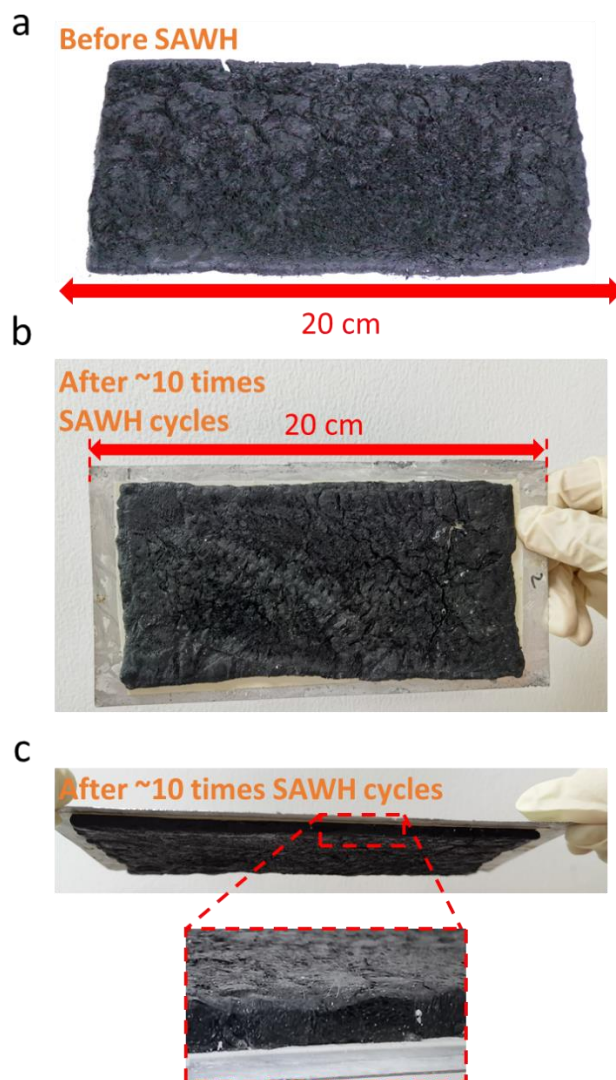


Figure S46. Optical photos showing the shape of the nanocomposite sorbent before and after ~10 times SAWH cycles in device.

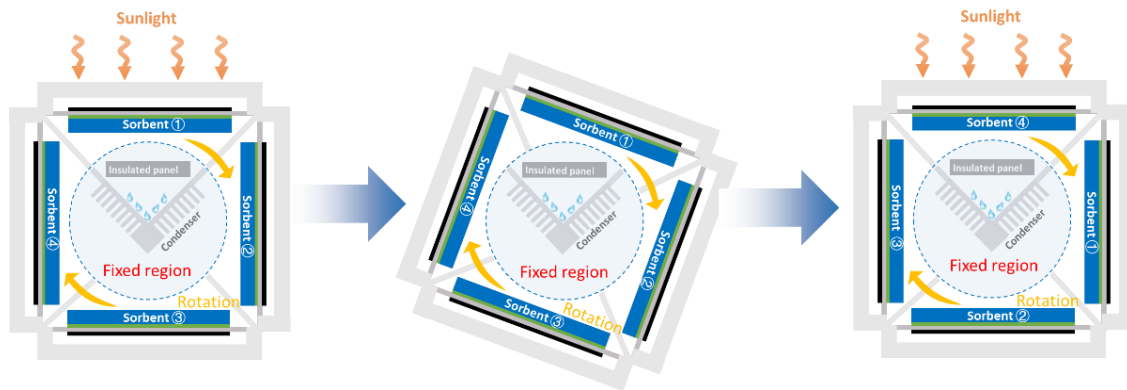


Figure S47. Schematic showing an automatic operation strategy for continuous water production.

We here provide one of possible ways to realize automatic operation of SAWH. The manual switching of sorbents can be replaced by mechanically rotation driven by PV-powered motor and auxiliary actuators. The condenser and insulated panel are fixed while the sorbents and solar absorber intermittently rotate for 90° during each switch process. Different from the manual switching, all the four sides need convective covers to reduce the heat loss during heat collection process. Since the forced air convection provides much higher heat convection coefficient than natural convection, the reduction of heat dissipation by extra convective covers is not remarkable. To realize successful SAWH, the seal components, located in the contact surface between fixed part and rotated part, need to be well designed to avoid the water vapor leakage in this rotational SAWH device.

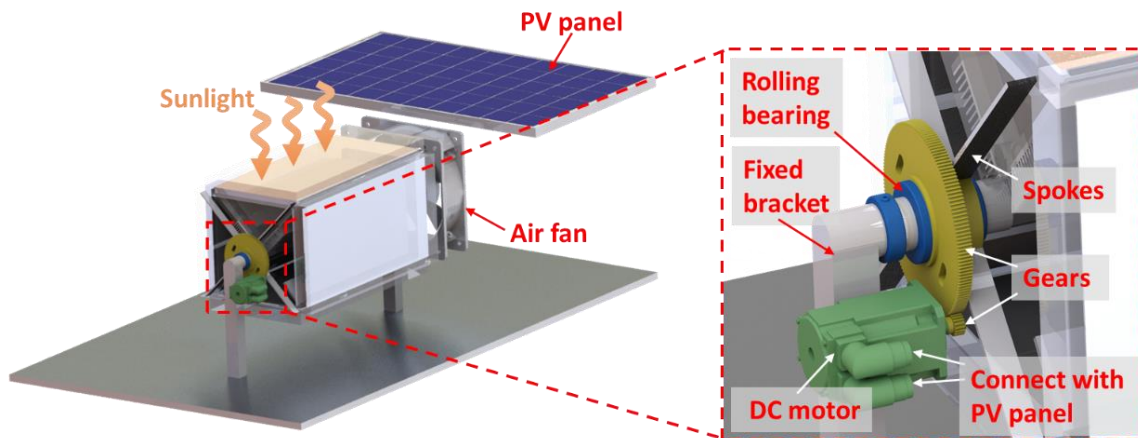


Figure S48. Schematic showing the automatic SAWH device with added mechatronic components.

To realize above automatic operation by periodically rotation, we here preliminarily provide one of possible solution. A PV-powered DC motor is employed to drive the rotation of gears. Then, the gears drive the rotation of spokes and shells of SAWH device, including solar absorber and sorbent. A control program should be embedded in to make the motor work periodically according to the desorption duration. In practical construction, the stability and reliability for mechatronic components should be well considered.

Table S1. The testing conditions of the LiCl@rGO-SA and other reported composite sorbent during the dynamic water sorption tested by commercial water sorption instrument.

	Temperature	Relative humidity
LiCl@rGO-SA (This work)	30 °C	30%
LiCl@rGO-SA_unordered	30 °C	30%
CaCl ₂ LiCl@FCNT	25 °C	20%
LiCl@ACF	25 °C	20%
LiCl@MIL-101(Cr)	30 °C	30%
LiCl@BCS	25 °C	40%
LiCl@HCS	25 °C	35%
CaCl ₂ @SA	30 °C	25%
LiCl@Graphene-NFC	25 °C	35%
CaCl ₂ @PAM-CNT	25 °C	35%

Table S2. Thermal efficient analysis for the SAWH device with/without insulation panel.

	Symbol	Unit	Value
Input solar flux	q_{solar}	W m^{-2}	1000
Reflectance + absorbance ratio	f	/	0.1
Absorptivity ratio of selective absorber	ε	/	0.92
Emissivity of acrylic cover	$\varepsilon_{\text{cover}}$	/	1
Convective heat transfer coefficient of acrylic cover to ambient	$h_{\text{conv, cover}}$	$\text{W m}^{-2} \text{K}^{-1}$	5
Convective heat transfer coefficient within condenser	$h_{\text{conv, condenser}}$	$\text{W m}^{-2} \text{K}^{-1}$	2
Thermal conductivity of air	λ_{air}	$\text{W m}^{-1} \text{K}^{-1}$	0.02
Thickness of air layer between sorbent and insulator	$\delta_{\text{air},1}$	mm	5
Ambient temperature	T_{amb}	$^{\circ}\text{C}$	30
External surface temperature of acrylic cover	$T_{\text{cover, out}}$	$^{\circ}\text{C}$	40
Condenser temperature, inner	$T_{\text{condenser}}$	$^{\circ}\text{C}$	42
Situation 1: Device without insulation panel between sorbent and condenser			
Temperature of sorbent, inner	T_{adsorb}	$^{\circ}\text{C}$	65
Radiative heat flux from cover to ambient	$q_{\text{radi, cover}}$	W m^{-2}	66.4
Convective heat flux from cover to ambient	$q_{\text{conv, cover}}$	W m^{-2}	50
Radiative heat flux from sorbent to condenser	$q_{\text{radi, condenser}}$	W m^{-2}	182.0
Convective heat flux within condenser	$q_{\text{conv, condenser}}$	W m^{-2}	46
Effective heat flux for water release	q_r	W m^{-2}	483.4
Calculated thermal efficiency*	η	%	48.3
Situation 2: Device with insulation panel between sorbent and condenser			
Temperature of sorbent, inner	T_{adsorb}	$^{\circ}\text{C}$	70
Temperature of Insulation panel, upper	$T_{\text{insul,up}}$	$^{\circ}\text{C}$	60
Radiative heat flux from sorbent to insulation panel	$q_{\text{radi, insul}}$	W m^{-2}	87.7
Conductive heat flux from sorbent to insulation panel	$q_{\text{cond, insul}}$	W m^{-2}	40
Effective heat flux for water release	q_r	W m^{-2}	584.9
Calculated thermal efficiency*	η	%	58.4

*The calculated thermal efficiencies are the theoretical values according to the heat transfer analysis in the desorption process. These values are higher than the practical thermal efficiency of 8 times SAWH cycles, 22.8%, calculated according to water amount. The difference between the theoretical thermal efficiency and practical thermal efficiency is majorly caused by the sensible heat losses during the frequently switching process of water sorption (cooling) and desorption (heating). This nonnegligible heat loss during switching process of rapid cycling SAWH system is unavoidable, telling us to optimized this part heat loss to a lower value, which will be considered in our future works.

Table S3. The mass and thickness of the four sorbent units in SAWH device.

	Unit 1	Unit 2	Unit 3	Unit 4
Mass of sorbent (g)	5.656	4.735	5.247	6.164
Total mass of sorbent, TIM, and selective absorber (g)	52.870	49.297	48.993	62.008
Thickness of TIM (mm)	0.12	0.12	0.12	0.12
Thickness of selective Absorber including the aluminum sheet (mm)	0.30	0.30	0.30	0.30
Thickness of sorbent (mm)	3.58	3.68	3.17	3.37

Table S4. The water harvesting capacity of the SAWH device in the view of sorbent, mass of device, volume of device, and solar collection surface of device.

	Absolute value (g/day)	Specific value per mass of sorbent (g/(g _{sorbent} ·day))	Specific value per mass of device ¹ (g/(kg _{device} ·day))	Specific value per volume ² (g/(L _{device} ·day))	Specific value per surface ³ (g/(m ² ·day))
Predicted monocyte AWH capacity under 15% RH at 30 °C	45.78	2.10	32.46	17.28	404.24
Predicted monocyte AWH capacity under 30% RH at 30 °C	67.15	3.08	47.62	25.34	593.33
Predicted monocyte AWH capacity under 60% RH at 30 °C	119.91	5.50	85.03	45.25	1059.39
Practical multicycling AWH capacity under indoor condition	46.42	2.13	32.91	17.52	1406.67
Practical multicycling AWH capacity under outdoor condition	22.82	1.05	16.18	8.63	691.52

1. The mass of device (1.41 kg) including the mass of sorbent, solar selective absorber, acrylic enclosure, condenser, solar PV, air fan, water tube, and water valve.
2. The volume of sorbent bed (2.65 L) refers to the volume of PV panel and the volume of air duct, where sorbent and condenser are both located on.
3. The surface of PV panel (0.013 m²) and solar selective absorber (0.02 m²). This area is the practical surface area of the device rather than the projected area.

Since the 6 W PV-powered fan can drive air flow in many of series-SAWH devices for its low flow resistance, a quarter of PV panel's area, weight, and volume are calculated in as the effective area, weight, and volume.

Table S5. Concentration of primary metal elements in collected water measured by ICP-OES.

	Concentration (mg/L)	Guideline from WHO (mg/L)
Li	0.533	N/A ¹
Na	1.138	50
Ca	5.424	200
Zn	0.156	3
Al	0.156	N/A ²
Cu	0.013	2
Pb	none	0.01
Fe	0.027	0.3

1. Although there is no guideline level for lithium in drinking water, long-term exposure to Li may be associated with adverse health effects.⁵ Even for treating depressive bipolar affective disorders, a low therapeutic dose range (300–2700 mg Li/day) was recommended from literature.⁶

2. Although there is no guideline level for aluminum in drinking water, it might accelerate the processes involved in Alzheimer's disease pathology, reported by some researchers.⁷

Considering the water quality may be affected by the outside environment (e.g., dusty, wind) and uncertainty operation condition (e.g., vibration), it is meaningful to further purify the collected water for decrease the metal concentration to a lower value. For example, install a water filter in the atmospheric water harvester to ensure the long-term safety of collected water. Recently, an omni-phobic fabric was reported to encapsulating the composite sorbent for screen out the contaminants, which can further insure the high quality of collected water.⁸

Table S6. Concentration of possible ions in collected water measured by Ion Chromatography.

	Concentration (mg/L)	Guideline from WHO (mg/L)
NH ₄ ⁺	4.726	N/A
F ⁻	1.165	1.5
Cl ⁻	3.450	250
SO ₄ ²⁻	0.411	500
Br ⁻	0.259	N/A
NO ₃ ⁻	0.439	50

References

1. J. Xu, T. Li, J. Chao, S. Wu, T. Yan, W. Li, B. Cao and R. Wang, *Angewandte Chemie International Edition*, 2020, **59**, 5202-5210.
2. J. Xu, T. Li, T. Yan, J. Chao and R. Wang, *Solar Energy Materials and Solar Cells*, 2021, **219**, 110819.
3. J. Y. Wang, R. Z. Wang, Y. D. Tu and L. W. Wang, *Energy*, 2018, **165**, 387-395.
4. I. K. Moon, J. Lee, R. S. Ruoff and H. Lee, *Nature Communications*, 2010, **1**, 1-6.
5. G. Concha, K. Broberg, M. Grandér, A. Cardozo, B. Palm and M. Vahter, *Environmental Science & Technology*, 2010, **44**, 6875-6880.
6. M. Krachler and W. Shotyk, *Science of the Total Environment*, 2009, **407**, 1089-1096.
7. E. Nieboer, B. L. Gibson, A. D. Oxman and J. R. Kramer, *Environmental Reviews*, 1995, **3**, 29-81.
8. R. Li, M. Wu, Y. Shi, S. Aleid, W. Wang, C. Zhang and P. Wang. *Journal of Materials Chemistry A*, 2021, **9**, 14731-14740